Pergamon

Geochimica et Cosmochimica Acta, Vol. 68, No. 13, pp. 2905–2923, 2004

0016-7037/04 $30.00 + .00

doi:10.1016/j.gca.2004.02.001

Oxygen isotopic SIMS analysis in Allende CAI: Details of the very early thermal history of the solar system

MOTOO ITO,[1,*] HIROSHI NAGASAWA,[1] and HISAYOSHI YURIMOTO[2]

[1]Department of Chemistry, Gakushuin University, Mejiro, Toshima-Ku, Tokyo 171-8588, Japan
[2]Department of Earth and Planetary Sciences, Tokyo Institute of Technology, Ookayama, Meguro-Ku, Tokyo 152-8551, Japan

(*Received July* 17, 2003; *accepted in revised form February* 2, 2004)

Abstract—The oxygen isotopic micro-distributions within and among minerals in a coarse-grained Ca, Al-rich inclusion (CAI), 7R-19-1 from the Allende meteorite, were measured by in situ using secondary ion mass spectrometry (SIMS). All values of O isotopic ratios in 7R-19-1 minerals fall along the carbonaceous chondrite anhydrous mineral mixing (CCAM) line on a $\delta^{17}O_{SMOW}$ vs. $\delta^{18}O_{SMOW}$ plot. Major refractory minerals (spinel, fassaite and melilite) in 7R-19-1 showed large negative anomalies of $\Delta^{17}O$ in the order, spinel (−21‰) > ^{16}O-rich melilite (∼−18‰) > fassaite (−15 to +1‰) > ^{16}O-poor melilite (−8 to +2‰). However, the lower limit values of $\Delta^{17}O$ are similar at about −21‰, a value commonly observed in CAIs. The similarity in the extreme values of the isotope anomaly anomalies suggests that crystallization of all CAIs started from an ^{16}O enrichment of 21‰ ($\Delta^{17}O$) relative to terrestrial values. The order of the O isotopic anomalies observed for 7R-19-1, except for ^{16}O-poor melilite, is parallel to the crystallization sequence determined by experiment from CAI liquid (Stolper, 1982), indicating that the O isotopic exchange in 7R-19-1 occurred between CAI melt and surrounding gas while 7R-19-1 was crystallizing from the ^{16}O enriched CAI liquid (∼−21‰ in $\Delta^{17}O$) in the ^{16}O-poor solar nebula. However, the a single crystallization sequence during the cooling stage cannot explain the existence of ^{16}O-poor melilite. The presence of ^{16}O-poor melilite suggests that multiple heating events occurred during CAI formation. The sharp contact between ^{16}O-rich and ^{16}O-poor melilite crystals and within ^{16}O-rich melilite indicates that these multiple heatings occurred quickly. Based on the O isotopic and chemical compositions, fassaite crystals were aggregates of relic crystals formed from CAI melt whichthat have had various O isotopic compositions from the remelting processes. The results of intra-mineral distributions of O isotopes also support multiple heating events during CAI formation. *Copyright © 2004 Elsevier Ltd*

1. INTRODUCTION

Ca, Al-rich inclusions (CAIs) are typically mm- to cm-sized objects found in various kinds of chondrites. CAIs are generally composed of melilite, pyroxene, and spinel with Ca- and Al-rich compositions. From the observed chemical and mineralogical compositions, CAIs are believed to be a very resistive material against the severe high-temperature conditions in the early solar nebula (Grossman, 1972). Chronological studies reveal that CAIs are the oldest known material from the early solar system (Allègre et al., 1995).

Oxygen isotopic anomalies in CAIs can be best expressed with the well-known three-isotope diagram ($\delta^{17}O$ vs. $\delta^{18}O$) of Clayton et al. (1973). The isotopic fractionation resulting from a normal chemical process depends on the mass differences among isotopes: the fractionation takes place along a line with a slope of ∼1/2 on the oxygen three-isotope diagram. The O isotope ratios ($^{18}O/^{16}O$ and $^{17}O/^{16}O$) of CAI minerals observed by Clayton et al. (1973) are distributed along a line called the "carbonaceous chondrite anhydrous minerals mixing (CCAM) line" having a slope of almost unity. In the three-isotope diagram, spinel was always the richest in the ^{16}O component, at about $\Delta^{17}O \approx -21$‰ relative to Standard Mean Ocean Water (SMOW), clino-pyroxene (fassaite) and olivine (forsterite) are next at $\Delta^{17}O \approx -15$‰, whereas melilite and anorthite are much less enriched in the ^{16}O component, normally at about $\Delta^{17}O \approx -4$‰ (Clayton et al., 1977; Clayton, 1993).

Rounded CAIs in the carbonaceous chondrites show textural and chemical evidence of having crystallized from a molten state as isolated droplets (Grossman, 1975). The existence of well-defined $^{26}Al/^{26}Mg$ isochrons in many of the CAIs indicates that the isotopic composition of Mg was initially uniform from mineral to mineral in these inclusions (MacPherson et al., 1995). Nevertheless, there are widely different O isotopic compositions distributed even within a single CAI, and most of the O isotopic ratios fall along the usual CCAM line on the O three-isotope plot. No process is known that could give rise to such isotopic distributions of O by closed-system crystallization in a melt. Furthermore, no element other than O shows such large anomalies and unusually heterogeneous intermineral distributions of stable isotopes.

To produce the observed correlation between mineralogy and isotopic composition, the following explanations have been proposed. One is that the isotopic exchange between the CAI liquid and the external O-bearing reservoir (e.g., surrounding nebular gas) was taking place during crystallization (Clayton, 1993). In this model, the early-crystallizing minerals (e.g., spinel) have isotopic compositions closer to that of the initial liquid (^{16}O-rich), whereas late-crystallizing minerals (e.g., plagioclase) have compositions close to the external reservoir (^{16}O-poor) (Stolper, 1982; Stolper and Paque, 1986). The difficulty with this model is that crystallization of melilite (^{16}O-

* Author to whom correspondence should be addressed, at Department of Geosciences, University of Arizona, Tucson, AZ 85721, USA (motoo@geo.arizona.edu).

poor) precedes that of pyroxene (^{16}O-rich). Therefore, O isotope exchange between melt and nebular gas during the cooling stage of CAIs does not explain the heterogeneous O isotope distribution.

An alternative explanation is that the observed heterogeneity of O isotopes was produced by gas-solid exchange after solidification of the CAI liquid (Clayton et al., 1977; Clayton and Mayeda, 1977). Here, the degree of O isotope exchange depends on the self-diffusion coefficients of O in the minerals: O of minerals with high O diffusion coefficients will have been equilibrated with the surrounding gas (^{16}O-poor), while O in minerals with low O diffusion coefficients retains its original isotopic composition (^{16}O-rich). For example, spinel, with a very small O self-diffusion coefficient (Ando and Oishi, 1974), retains its initial ^{16}O-rich composition, while melilite, with a large diffusion coefficient, exchanges extensively with the ^{16}O-poor external reservoir. Hayashi and Muehlenbachs (1986) reported that O diffusivity in melilite is much higher than in pyroxene and spinel. However, Yurimoto et al. (1989) and Ryerson and McKeegan (1994) determined O diffusion coefficients in synthetic åkermanite and gehlenite, and concluded that in melilite they are at least two orders of magnitude lower than those reported by these authors. The diffusion studies of Yurimoto et al. (1989) and Ryerson and McKeegan (1994) indicate that it is difficult to explain observed O isotopic distributions among CAI minerals by solid-gas diffusive exchange.

Intracrystalline O isotopic distributions in CAI minerals are homogeneous and this is preserved at the grain boundaries between minerals having independent O isotopic ratios (Yurimoto et al., 1994). This result confirms that partial exchange of O isotopes in the Allende CAI with the surrounding nebula gas through the diffusion process is also unlikely as an origin for the observed intermineral heterogeneity of O isotopes. Yurimoto et al., (1994) concluded that the heterogeneous O isotopic distribution among the minerals was established during crystallization.

Yurimoto et al. (1998) reported that in CAI 7R-19-1, coexisting ^{16}O-rich and ^{16}O-poor melilite grains were in direct contact. They proposed that (1) the ^{16}O-rich CAI originally crystallized from an ^{16}O-rich partial liquid droplet in the solar nebula, (2) the original CAI was melted during subsequent reheating events in the solar nebula, and (3) O isotopic exchange with the surrounding ^{16}O-poor nebular gas progressed through the resolidification of the CAI.

In this work, we report full chemical and petrographic studies of CAI 7R-19-1, with more detailed analyses of O isotopic inter/intramineral distributions than presented by Yurimoto et al. (1998). The objective was to construct a model of CAI formation constrained by thermal events in the early solar system as implied by our new data and the previous data for 7R-19-1.

2. EXPERIMENTAL METHODS

2.1. Scanning Electron Microscopy

Backscattered electron images, digital X-ray maps, and quantitative chemical analyses were obtained from three polished sections of Allende CAI 7R-19-1 with an Hitachi S-2400 scanning electron microscope (SEM) equipped with an Horiba E-MAX 7000 energy-dispersive X-ray microanalysis system (EDX) at Gakushuin University. For each quantitative chemical analysis, data for major elements were collected at 20 keV with a beam current of ~1 nA and a measurement time of 100 s for each point. Data were reduced via the ZAF correction installed in the EDX system. Total weight percent was normalized to 100%. Relative accuracies of abundances are estimated to be ~8 C.V.%.

2.2. Oxygen Isotopic Measurement by SIMS

O isotopic ratios were measured by the TiTech CAMECA ims-1270 SIMS instrument on 30 nm Au-coated polished samples utilizing a high mass resolution technique. The primary ions were mass-filtered positive ^{133}Cs accelerated to 20 keV, with a beam spot size of 3 to 5 μm in diameter. A primary current of 2 to 5 pA was adjusted for each measurement to obtain count rates of negative ^{16}O secondary ions of $(4.0 \pm 0.2) \times 10^5$ counts $\cdot$ s^{-1} (cps). A normal-incident electron gun was utilized for charge compensation of the analysis area. The transfer optics of the instrument were adjusted to obtain an imaged field of 150 μm and the mass spectrometer was set to XY mode (De Chambost et al., 1991). The field aperture and the energy slit were set to a width of 20 μm in the field image with an energy window of $\pm$ 75 eV. A contrast aperture of 400 μm was used and the entrance slit (20 μm width) and exit slit (150 μm width) of the mass spectrometer were narrowed enough to obtain the required mass resolution ($M/\Delta M > 6000$ at 10% peak width) for separation of ^{17}O$^-$ and ^{16}OH$^-$ mass peaks. The ^{16}OH$^-$ signal is often 2–3 orders of magnitude larger than the ^{17}O$^-$ signal, which is due to using a small primary beam size with the low beam current. The ^{16}OH$^-$ signal was mainly generated from the rim of the irradiated area of the primary beam.

Negative secondary ions of $^{16}O_{tail}$ (15.991520 amu), ^{16}O (15.994915 amu), ^{17}O (16.999131 amu), ^{16}OH (17.002740 amu) and ^{18}O (17.999160 amu) were analyzed in this sequence. The $^{16}O^-_{tail}$ and ^{16}OH$^-$ signals were measured for the purpose of correcting the remaining interference of the ^{16}OH$^-$ component with the ^{17}O$^-$ peak. The interference correction was always less than 0.6‰ in the δ^{17}O notation, even if the ^{16}OH$^-$ signal was three orders of magnitude larger than the ^{17}O$^-$ signal. Each measurement was conducted with 100 cycles of counting the $^{16}O_{tail}$ for 5 s, ^{16}O$^-$ for 2 s, ^{17}O$^-$ for 7 s, ^{16}OH$^-$ for 2 s and ^{18}O$^-$ for 3 s, and lasted for 45 min. Each run was started only after stabilization of the secondary ion beam following presputtering. The sputtered area after measurement consisted of a 3–5 μm crater $\leq$ 1 μm in depth surrounded by a halo. Secondary ions were mainly generated from the inside of deep craters of 3–5 μm diameter on the sample surface.

Secondary ions were detected by a Balzers electron multiplier (EM) operated in a pulse counting mode, with corrections for dead time (21.2 $\pm$ 0.8 ns) based on measurements of a spinel standard, SPU (spinel from Russia), under similar conditions as used for the samples.

The matrix effect, which may cause systematic intermineral errors, can be checked by comparing the analytical results for terrestrial analogues. For the purpose of estimating the matrix effect and instrumental mass fractionation, we measured oxygen isotope ratios of terrestrial standards with known oxygen isotopic ratio (Yurimoto et al., 1994), SPU (spinel from Russia), anorthite (Miyake-Jima, Japan), augite (Takashima, Japan), synthetic gehlenite and synthetic åkermanite. The reproducibility of $^{17,\ 18}$O/^{16}O on different analyses of the same standard was within ~5‰ (1σ). The matrix effect of O isotopic analysis among these minerals was less than 5‰ (1σ) under the analytical conditions. Overall errors in the observed results are estimated to be ~5‰ for each analysis (Ito, 1999).

An average isotope ratio of the SPU standard was used to determine $\delta^{17,\ 18}O_{SMOW}$ values for corresponding unknown samples. The $\delta^{17,\ 18}O_{SMOW}$ values were calculated as follows:

$$(\delta^{17or18}O_{SMOW})_{uk} = (\delta^{17or18}O_{SMOW})_{st} + (R_{uk}/R_{st} - 1) \times 1000 \text{ [permil]}$$

where R is the measured isotope ratio of $^{17,\ 18}$O/^{16}O and subscripts uk and st correspond to unknown and standard samples, respectively. For calculating isotopic ratios, the intensities were linearly interpolated in time.

Because submicron spinel grains were scattered in some areas of ^{16}O-rich Mel* crystals (^{16}O-rich melilite crystal, see in Fig. 1), to check possible contamination of the spinel, careful observations by high-

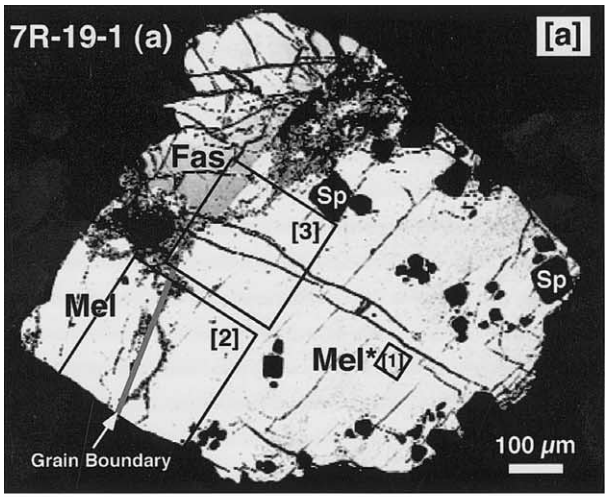

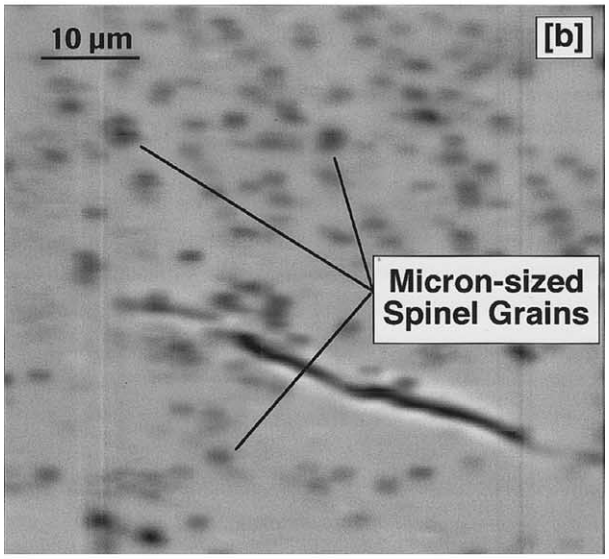

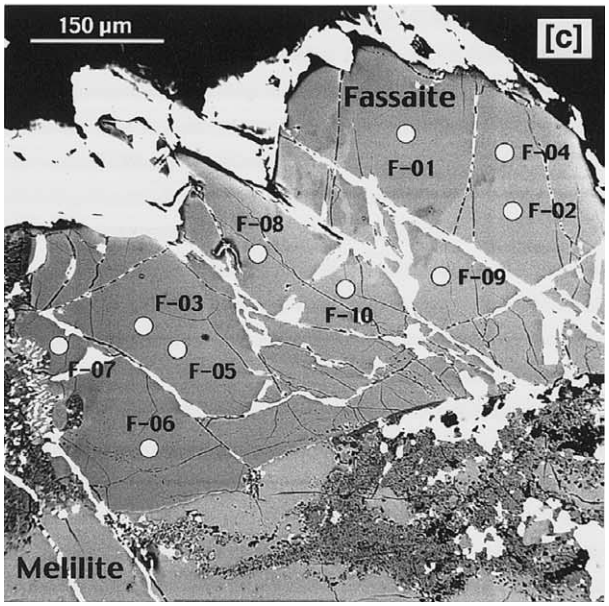

magnification photographs (optical and backscattered electron images) have been made within and around the ion probe craters in ^{16}O-rich melilite. We confirmed that all O isotopic data in this study were collected from a monomineralic phase. Data from polymineralic phases due to the effect of primary beam overlapping were rejected.

3. RESULTS

3.1. Petrography and Bulk Chemical Composition

The sample used in this study, 7R-19-1, consists of a coarse-grained CAI separated from the Allende CV3 meteorite specimen 7R-19 provided by Dr. Elbert King. The 7R-19-1 coarse-grained CAI appears originally to have had a round shape with ~5 mm radius, estimated from the curvature of the CAI edge. However, this specimen was broken during laboratory handling. Five polished sections were prepared from the pieces of 7R-19-1, and are designated as (a), (b), (c), (d) and (e), of which (a), (d) and (e) were used in this study. Section (a) is from the center whereas (d) and (e) are from the edge of the CAI. All three pieces consist of melilite, fassaite and spinel as major minerals. The size and occurrences of these minerals are similar in the three pieces.

The cross section of 7R-19-1(a) is 1.4 mm square (Fig. 1 [a]). The melilite consists of two-grains, named Mel (0.4 × 0.3 mm) and Mel* (1.4 × 1 mm). Spinel grains of square or small-rounded shape (10 to 100 μm) are scattered in Mel* (Fig. 1 [a]). Micron-sized spinel grains (< ~2 μm in diameter) were also observed in Mel* (Fig. 1). The large angular fassaite crystal is 0.6 × 0.3 mm in size (Fig. 1 [c]). Small, rounded fassaite grains (~30 μm in diameter) were observed in both melilite crystals.

Sector-shaped 7R-19-1(d) is the largest piece of 7R-19-1, and is 3 × 3 mm in size (Fig. 2 [a]). Many melilite crystals (200–300 μm in size) found in 7R-19-1(d) are lath shaped. Only the melilite grain in the hibonite-rich center area grain has an irregular outline (Figs. 2 [a,d]). Some melilite-melilite contacts are planar and others are sutured. The large angular fassaite crystals (0.8 × 0.5 mm square) have sector and growth zoning (Fig. 2). A smaller, angular fassaite crystal (0.4 × 0.2 mm) is also observed (Fig. 2 [a]), and very small rectangular fassaite crystals (20 × 10 μm) are observed in spinel grains. This fassaite grain has distinct O isotopic ratios discussed in the following section (sec. 3.3.2). Spinel grains generally are euhedral and 20–100 μm in size, and are poikilitically enclosed in melilite crystals. The center area of 7R-19-1(d) is composed of irregularly shaped aggregates of melilite, fine-grained perovskite, irregularly shaped hibonite (40 × 20 μm) and alteration products with rough surfaces (Fig. 2 [c]). A Wark-Lovering rim exists on the circumference of the 7R-19-1(d) with sector form. The rim consists of a ~50 μm layer of irregularly

Fig. 1. [a] Backscattered electron image of 7R-19-1(a). This fragment is collected from the central part of the CAI. Boxed areas [1], [2], and [3] correspond to Figures 1, 9, and 10, respectively. Backscattered electron image of small-rounded spinel grains (black points, 2–3 μm in diameter) in the ^{16}O-rich melilite crystal of 7R-19-1(a). [c] Backscattered electron image of angular fassaite in 7R-19-1(a). Circles show locations of the SIMS analysis with the analysis number given in Table 7. The white region along crystals is a thin film of gold, which was not removed by polishing. Sp = spinel; Mel = ^{16}O-poor melilite; Mel* = ^{16}O-rich melilite.

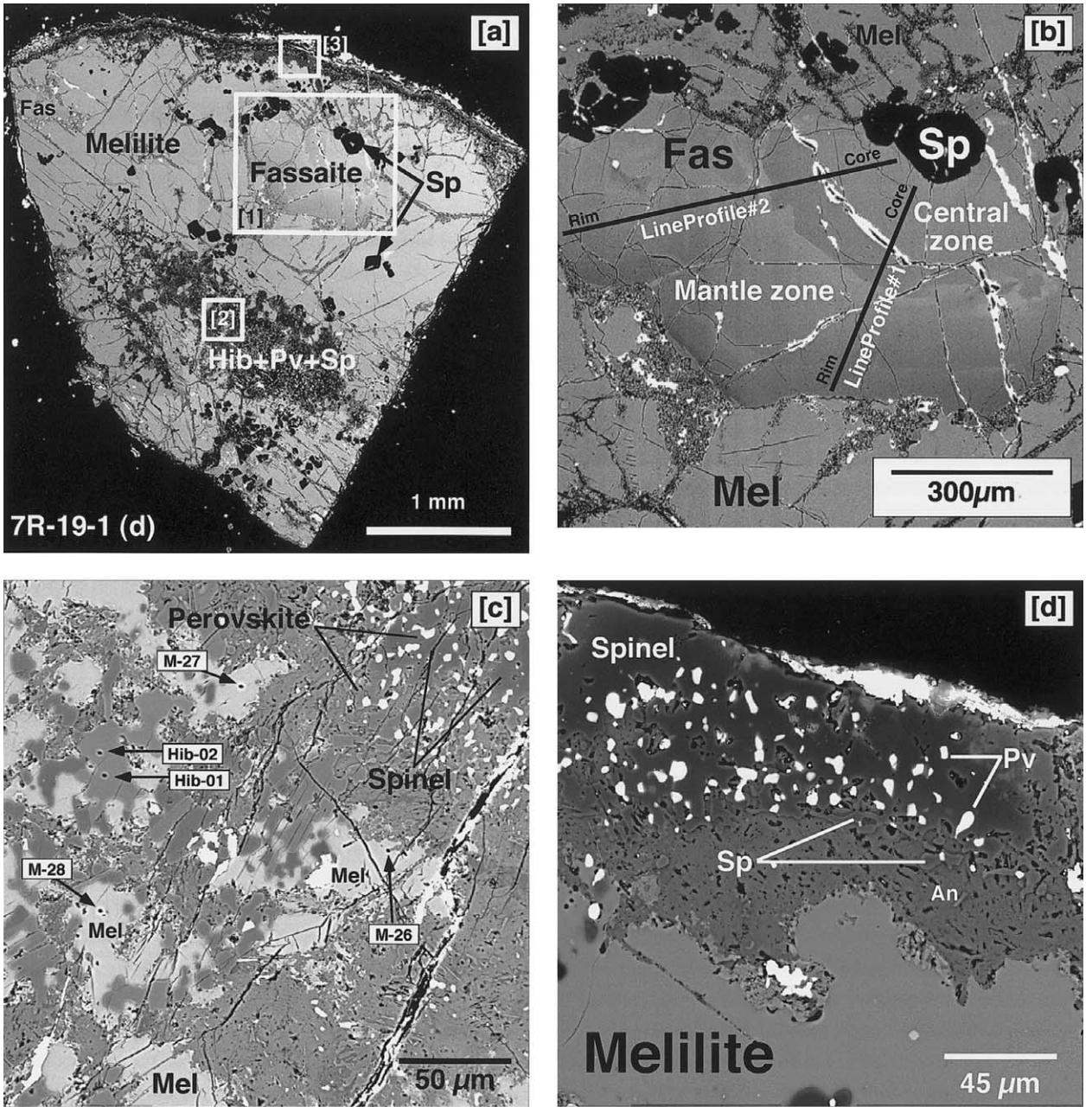

Fig. 2. [a] Backscattered electron image of 7R-19-1(d). The fragment retains parts of the rim of its original CAI, enriched in spinel and fine-grained perovskite. Small rectangular fassaite is visible in the upper left of the sample. Boxed areas [1], [2], and [3] correspond to Figure 2, [c] and [d], respectively. Backscattered electron image of the large angular fassaite in the 7R-19-1(d). The fassaite has sector and growth zoning. The positions of line profiles 1 and 2 are shown by lines and were obtained from stepped traverses within the fassaite crystal. The O isotopic measurements for line profiles consisted of 13 points at intervals of ~32 μm along line 1, and of 19 points at intervals of ~35 μm along line 2. [c] Backscattered electron image of the center area of 7R-19-1(d). Brightest spots are perovskite and the dark area near the perovskite is spinel. The white area is melilite; the irregularly shaped gray area is hibonite. Gray, loosely coagulated crystals with rough surfaces are alteration products. M-26 to 28 and Hib-01 to 02 indicate the SIMS analysis locations shown in Tables 6 and 9. [d] Backscattered electron image of rim structure of the original CAI in polished section 7R-19-1(d). The rim is composed of spinel, perovskite, melilite; and alteration products (anorthite; Fe-rich spinel; and altered melilite). Mel = melilite; Sp = spinel; Fas = fassaite; Hib = hibonite; Pv = perovskite; An = anorthite.

shaped spinel and fine-grained perovskite (Fig. 2 [d]). The intermediate zone between melilite and the spinel + perovskite layer in the rim is composed of the alteration products anorthite, Fe-rich spinel and altered melilite. Anorthite crystals in the rim are needle-shaped and are ~5 μm in length (Fig. 2 [d]). Perovskite is present mostly as fine, rounded shapes ~5 μm in diameter in the central and rim areas (Figs. 2 [c,d]).

The size of 7R-19-1(e), a half-circle–like form is 3 × 2 mm

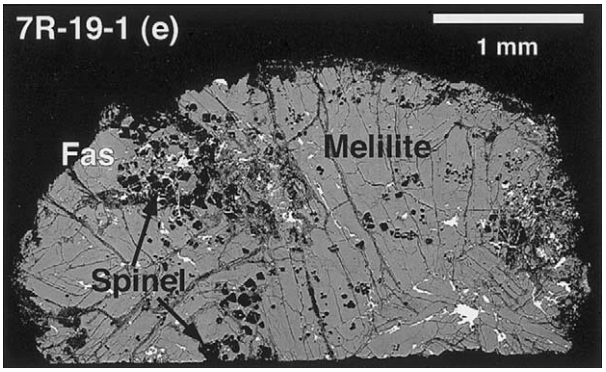

Fig. 3. Backscattered electron image of 7R-19-1(e). The fragment retains parts of the rim of its original CAI, enriched in spinel and fine-grained perovskite. Fas = fassaite.

(Fig. 3). 7R-19-1(e) consists of many crystals of melilite, fassaite and spinel with small amounts of perovskite in the rim. Melilite crystals are similar to those in 7R-19-1(d). The fassaite crystal is 0.5 × 0.4 mm square. Spinel grains are square ~10–100 μm across in the melilite and fassaite crystals. The interior textures and rim of 7R-19-1(e) are similar to those of 7R-19-1(d).

In summary, the three pieces of the 7R-19-1 sample mainly consist of melilite ($Åk_{13–30}$, roughly 60 ~ 70 vol%), fassaite (~ 10 vol%) and spinel (~ 10 vol%) grains. Minor mineral phases are hibonite and perovskite. Alteration products (mainly anorthite and grossular) are present along some grain boundaries, cracks and the rim.

Although the mineral assemblage of this CAI corresponds to those of Type B (Grossman, 1975), it does not have the concentrically zoned structure with a melilite mantle as normally seen for the Type B1 CAI's. The petrographic texture and mineral composition of 7R-19-1 may correspond to those of coarse-grained melilite-rich Type B2 or fassaite-rich compact Type A CAI's (MacPherson et al., 1988; Simon et al., 1995). The euhedral textures suggest that 7R-19-1 crystallized from a melt, and thus represents a primary coarse-grained CAI.

The bulk chemical composition of 7R-19-1 was determined as the average chemical composition of eight rastered-beam areas (750 μm square; there is some overlap in the areas) using SEM-EDX analysis (Table 1). Figure 4 shows the liquidus phase relationships as projected from spinel onto the plane of the anorthite-gehlenite-forsterite system (Stolper, 1982; Stolper and Paque 1986). Two analyses plot away from the others, but

Table 1. Bulk chemical compositions of 7R-19-1.

	7R-19-1 (wt%)	1σ[a]
MgO	7.1	2.7
Al_2O_3	36.3	5.6
SiO_2	24.1	3.0
CaO	30.7	4.7
TiO_2	1.7	2.1
FeO	0.3	0.5
Total	100	

[a] Standard deviations of eight measurements.

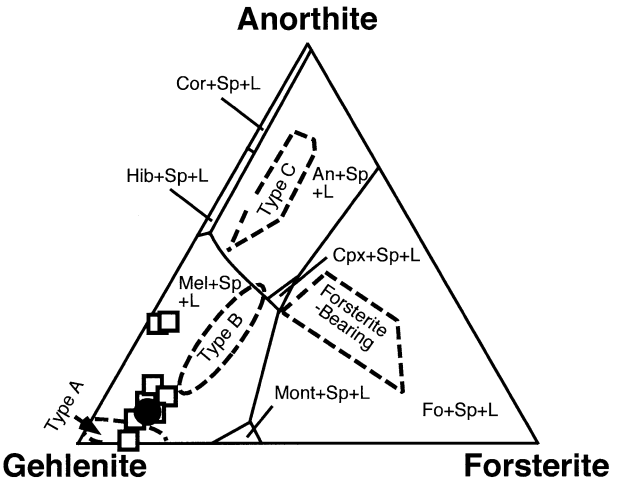

Fig. 4. Bulk composition of CAI 7R-19-1 (solid circle = average of eight points; open squares = individual measured points) plotted on liquidus-phase relationships as projected from spinel onto the plane anorthite-gehlenite-forsterite (Stolper, 1982). Dashed lines enclose the observed bulk-composition areas of the principal CV3 coarse-grained inclusion types (Wark 1981, 1987; Beckett, 1986; Wark et al., 1987; MacPherson et al., 1988). 7R-19-1 (solid circle) falls near the composition of Type A CAIs.

these were obtained in areas dominated by fassaite. Six data points fall in the Type A area (open squares: individual data points, solid circle: average of eight points). The bulk chemical composition of 7R-19-1 (solid circle) falls near the compositional area of Type A CAIs.

3.2. Mineral Chemistry

3.2.1. Melilite

Generally, melilite in CAIs can be considered as a binary solid solution between åkermanite ($Ca_2MgSi_2O_7$) and gehlenite ($Ca_2Al_2SiO_7$). Chemical compositions of melilite crystals in 7R-19-1 were determined in randomly selected spots. For all melilite analyses, the numbers of cations were calculated on the basis of seven oxygen atoms. Table 2 summarizes selected individual data points for representative compositions, and all data are summarized in Figure 5 as a histogram (over 100 measured points for each section). 7R-19-1(a), which consists of two crystals, shows a sharp peak throughout at $Åk_{23}$ while 7R-19-1(d) and (e), which consist of many dispersed crystals show broad peaks at ~$Åk_{17}$. Based on the histogram shown in Figure 5, åkermanite compositions of melilite in 7R-19-1 are similar to those of Type A CAIs (Grossman, 1975).

3.2.2. Fassaite

Representative compositions of fassaite in 7R-19-1(a) and (d) are summarized in Table 3, where all Ti is assumed to be Ti^{4+}. The numbers of cations are calculated on the basis of six oxygen atoms. Contents of Al_2O_3 and TiO_2 in fassaite crystals of 7R-19-1(a) are 19 ~23 wt% and 11 ~20 wt%, respectively. The contents of Al_2O_3 and TiO_2 in fassaite crystals of 7R-19-1(d) are 17 ~27 wt% and 12 ~21 wt%, respectively. Small, rounded, fassaite grains in Mel (^{16}O-poor melilite) and Mel*

Table 2. Representative analysis of melilite in 7R-19-1 (wt%).

	7R-19-1 (a)				7R-19-1 (d)				7R-19-1 (e)	
	Mel*[a]		Mel[b]				åk-rich			
	1	2	1	2	1	2	1	2	1	2
MgO	2.1	2.4	2.6	3.9	3.8	2.0	12.4	10.2	2.9	2.6
Al_2O_3	33.1	30.5	33.8	30.7	32.0	34.5	10.0	15.6	31.8	32.8
SiO_2	24.6	26.1	24.1	25.5	24.3	23.5	36.7	33.2	24.1	23.7
CaO	40.3	41.1	39.5	39.9	40.0	40.0	40.8	41.0	41.2	40.9
Total	100	100	100	100	100	100	100	100	100	100
	Cations per 7 oxygen anions									
Mg	0.14	0.16	0.17	0.27	0.25	0.14	0.85	0.69	0.2	0.17
Al	1.77	1.64	1.81	1.65	1.72	1.85	0.54	0.84	1.72	1.77
Si	1.12	1.19	1.09	1.16	1.11	1.07	1.68	1.52	1.1	1.09
Ca	1.96	2.00	1.92	1.94	1.95	1.95	2.00	2.01	2.02	2.00
Total	4.99	4.99	4.99	5.02	5.03	5.01	5.07	5.06	5.04	5.03
Åk	14	17	16	25	23	13	76	62	21	17

[a] Mel* = ^{16}O-rich melilite.
[b] Mel = ^{16}O-poor melilite.

(^{16}O-rich melilite) crystals are similar in chemical compositions to angular fassaite grains in 7R-19-1(a) (Table 3). Large and small angular fassaite and small rectangular fassaite surrounded by spinel in 7R-19-1(d) are of similar chemical composition (Table 3).

The major cations of fassaite are Ca, Al, Ti, Mg and Si. For the fassaite crystals in 7R-19-1(a) and (d), MgO is plotted vs. SiO_2 and Al_2O_3 in Figure 6 [a]. MgO and SiO_2 abundances are strongly correlated, while MgO and Al_2O_3 are strongly anticorrelated. 7R-19-1(a) and (d) have clearly separate trends of MgO vs. SiO_2 and Al_2O_3. In a plot of MgO vs. TiO_2 (Fig. 6 [c]), the Ti abundances decreases with increasing MgO abundances, and samples (a) and (d) form a single trend. Fassaite crystals in 7R-19-1(d) have higher TiO_2 abundances and lower Al_2O_3 abundances than those in 7R-19-1(a). This reverse correlation is explained by the exchange reactions, $Ti^{3+} + {}^{IV}Al^{3+} \leftrightarrow Mg^{2+} + Si^{4+}$ and $Ti^{4+} + 2{}^{IV}Al^{3+} \leftrightarrow Mg^{2+} + 2Si^{4+}$, where ^{IV}Al refers to Al in the tetrahedral site. Al also enters pyroxene as Tschermark's molecule via the reaction $^{IV}Al^{3+} + {}^{VI}Al^{3+} \leftrightarrow Mg^{2+} + Si^{4+}$ (Simon et al., 1991). These plots show that 7R-19-1(a) and (d) have clearly separate trends (Fig. 6 [a]) but the samples form a single trend in Figure 6 [c]. The trends may refer to different growth sectors because sector zoning is commonly well developed in fassaite crystals in CAIs (Davis et al., 1991). In a plot of SiO_2vs. TiO_2 (Fig. 6 [d]), the correlation of SiO_2vs. TiO_2 in the fassaites in 7R-19-1(a) and (d) correspond to those in Type A CAIs (Simon et al., 1999), indicating 7R-19-1 may be classified as a compact coarse-grained Type A CAI.

Compositional zoning in the large angular fassaite in 7R-19-1(d) (Fig. 2) consists of a central zone and a mantle zone. SEM-EDS traverse analyses across the zoning show an abrupt change of MgO, SiO_2, Al_2O_3 and TiO_2 concentrations at the boundary between the central and mantle zones (shown by arrows in Fig. 7). Trends of MgO, SiO_2, Al_2O_3 and TiO_2 within the central zone are similar to those within the mantle zone. The fassaite crystal exhibits an increase in MgO and SiO_2 from core to rim, while TiO_2 and Al_2O_3 decrease in abundance and CaO is constant from core to rim in both zones (Fig. 7).

3.2.3. Spinel

We analyzed chemical compositions of both blocky and irregular spinel grains in 7R-19-1(d). Representative compositions are summarized in Table 4 for blocky spinel, and for irregular-shaped spinel both in the central area and the rim. The numbers of cations were calculated on the basis of four oxygen atoms. Blocky spinel grains, which are scattered in melilite crystals, are nearly pure $MgAl_2O_4$. Some spinel grains included rectangular fassaite crystals (20 × 10 μm), and their chemical compositions are similar to those of the blocky spinel grains. Diffusion profiles of Fe were observed in some of the spinel grains. Irregular spinel crystals in the center of 7R-19-1(d), some with small rounded perovskite, have CaO (~2 wt%), TiO_2 (~2 wt%) and FeO (~4 wt%), while those in the rim have CaO (~5 wt%), TiO_2 (~6 wt%) and, FeO (~6 wt%) (Table 4). Usually spinel contains CaO in trace amounts of < 1 wt% (Grossman, 1975). Therefore, the relatively large amount of CaO we measure in irregular spinel possibly could be due to beam overlap or some convolution effect arising from measuring adjacent perovskite.

3.2.4. Accessory minerals (hibonite, anorthite, and perovskite)

Table 5 summarizes some representative compositions of hibonite [$Ca(Al,Ti,Mg)_{12}O_{19}$] crystals present in the center of 7R-19-1(d) (Fig. 2 [c]). The hibonite crystals contain MgO (~5 wt%), SiO_2 (~2 wt%) and TiO_2 (~6 wt%).

Some representative compositions of fine-grained (<5 μm) anorthite crystals [$CaAl_2Si_2O_8$] observed as an alteration phase along some grain boundaries (Fig. 2 [d]) in 7R-19-1(d) are listed in Table 5. The composition is nearly pure anorthite ($An_{95–100}$: average An_{99}).

Some representative compositions of fine perovskite grains [$CaTiO_3$] found in the center (Fig. 2 [c]), the rim area (Fig. 2 [d]) and around the spinel crystals of 7R-19-1(d) are summarized in Table 5. This phase is nearby pure $CaTiO_3$, with MgO

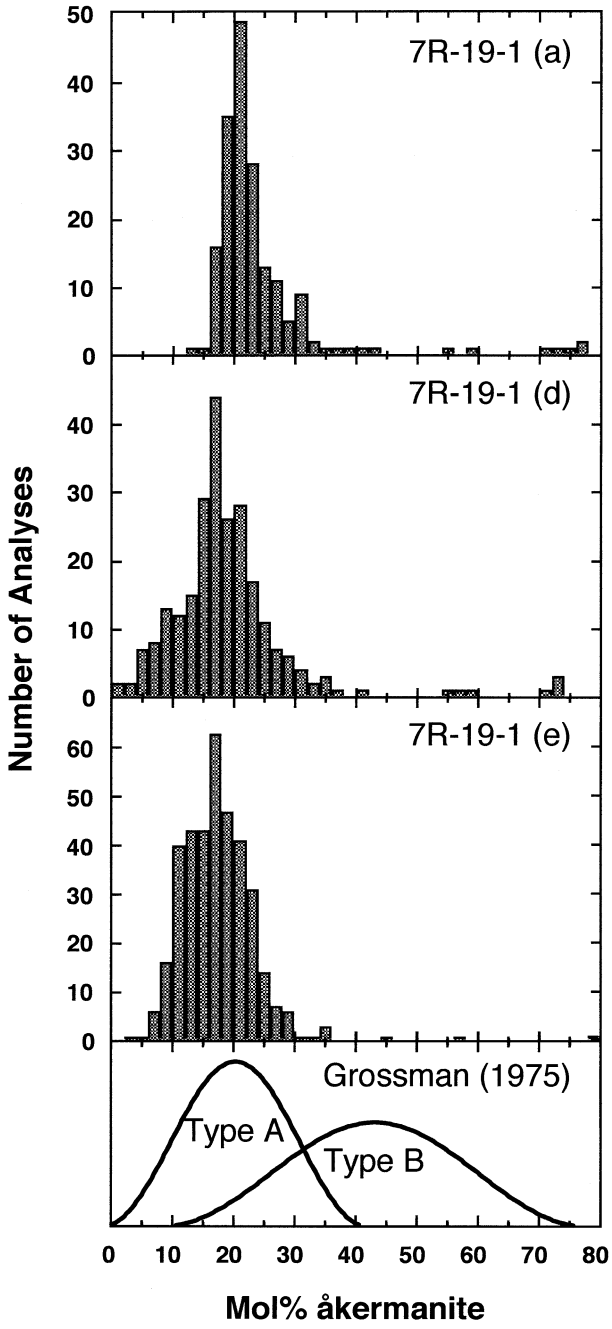

Fig. 5. Histograms of melilite composition (åkermanite mol%) in 7R-19-1(a), (d), and (e), together with observed åkermanite contents of Type A and B in Allende inclusions (Grossman, 1975). The histogram for the melilite in 7R-19-1(a) has a sharp peak in frequency between Åk18 and Åk23; in 7R-19-1(d) and (e) there is a broad peak between Åk13 and Åk25, and Åk10 and Åk23, respectively.

(~1 wt%), and Al_2O_3 (~6 wt%). SiO_2 ranges up to 3 wt% but reaches such a high value only in one case (Table 5).

Some of the data for hibonite and perovskite have small amounts of TiO_2, SiO_2 and MgO (Grossman, 1975). These contaminations could be due to some convolution effect during the measurement from surrounding minerals, i.e., fassaite, melilite.

3.3. Oxygen Isotopes

The distributions of O isotopic composition in the 7R-19-1 constituent minerals are summarized in Tables 6 to 9. Calculated errors indicated on the tables represent standard errors (1σ), which were calculated from the standard deviations of measurement cycles. These results are also plotted in three-isotope diagrams, which are shown in Figures 8 [a–d]. The data points fall on the CCAM line and are apparently in agreement with previous observations on normal coarse-grained CAIs. The degree of the ^{16}O excess can be shown by $\Delta^{17}O$ values ($\Delta^{17}O = \delta^{17}O - \delta^{18}O \times 0.52$), which are used for discussion in this paper (with a few exceptions). Errors for $\Delta^{17}O$ are calculated by error propagation of 1σ errors of $\delta^{17}O$ and $\delta^{18}O$.

3.3.1. Melilite

3.3.1.1. 7R-19-1(a). The $\Delta^{17}O$ values of the Mel crystal range from −8‰ to +2‰ and those of the Mel* crystal range from −25‰ to −13‰ (Table 6). A line profile of O isotopic distributions was obtained from stepped traverses across the boundary of the Mel (^{16}O-poor melilite) and Mel* (^{16}O-rich melilite) crystals (Fig. 9), and another one within the Mel* crystal near the angular fassaite crystal (Fig. 10). The grain boundary between Mel and Mel* was determined by the trend of åkermanite zoning in the crystal and cleavage orientation. The O isotopic measurement for line profiles consists of 6–10 points spaced at intervals of 5–25 μm depending on the O isotopic variations between adjacent points.

The O isotopic compositions of $\delta^{17,\,18}O$ are homogeneous in the Mel* crystal at about ~ −38‰, and abruptly changes to ~ −10‰ at the Mel* crystal rim inside of the Mel crystal (Fig. 9, Table 6). Åkermanite content gradually increases from $Åk_{20}$ to $Åk_{30}$ towards the grain boundary. The O isotopic boundary between ^{16}O-poor and ^{16}O-rich zones is not exactly at the grain boundary of the two melilite crystals but is ~100–120 μm from the grain boundary.

The line profile within the Mel* crystal near the angular fassaite crystal (Fig. 10) shows, correlated with a gradual increase in åkermanite content from $Åk_{20}$ to $Åk_{80}$, a change of O isotopic ratios from −35‰ to −10‰ in $\delta^{17,\,18}O$ (Fig. 10 and Table 6). The boundary between ^{16}O-poor and ^{16}O-rich regions is within the Mel* ~100–120 μm from the crystal's edge. These observations indicate that ^{16}O-poor melilite was overgrown directly on the ^{16}O-rich melilite grains.

3.3.1.2. 7R-19-1(d). 7R-19-1(d) consisted of many coarse-grained melilite crystals (Fig. 2 [a]). The $\Delta^{17}O$ values of these melilites range from −19‰ to +7‰ (Table 6). Melilite in the center and the rim area with complex texture shows ^{16}O-poor isotopic compositions (Figs. 2 [c,d], Table 6). Also, melilite that is close to hibonite grains has an ^{16}O-poor isotopic composition (Fig. 2 [c], Table 6, d_M-26 to 28). Within each melilite grain, O isotopic distributions are homogeneous (e.g., g#1 as d_M-02 and 03; g#2 as d_M-08, 09, 41, 62, and 83; g#3 as M-23 and 24; in Fig. 8 [a] and Table 6).

3.3.1.3. 7R-19-1(e). O isotopic compositions in 7R-19-1(e) are different from those in 7R-19-1(d) and show a bimodal ^{16}O-rich/^{16}O-poor distribution. Almost all melilite crystals show a large negative anomaly: $\Delta^{17}O$ values of ^{16}O-rich melilite range from −20‰ to −10‰ (Table 6). A small amount

Table 3. Representative analysis of fassaite in 7R-19-1 (wt%).

	7R-19-1 (a)					7R-19-1 (d)				
	Angular					Large angular				
	1	2	3	Small in Mel*[a]	Small in Mel[b]	1	2	3	Small angular	Fas in spinel
MgO	7.9	8.4	8.6	6.2	7.1	5.1	5.7	5.8	7.5	10.4
Al_2O_3	22.6	22.3	22.0	21.1	22.2	20.1	19.7	19.3	17.3	27.4
SiO_2	31.6	32.5	33.1	28.4	31.6	30.1	30.8	31.3	34.3	31.8
CaO	22.3	22.3	21.6	24.8	27.9	24.6	24.5	24.7	24.6	18.7
TiO_2	15.6	14.5	14.7	19.6	11.3	20.1	19.4	19.0	16.3	11.7
Total	100	100	100	100	100	100	100	100	100	100
	Cations per 6 oxygen anions									
Mg	0.44	0.46	0.47	0.35	0.40	0.29	0.32	0.32	0.42	0.56
Al	0.99	0.97	0.95	0.94	0.98	0.89	0.87	0.85	0.76	1.17
Si	1.17	1.20	1.22	1.07	1.19	1.13	1.15	1.17	1.28	1.15
Ca	0.88	0.88	0.85	1.00	1.12	0.99	0.98	0.99	0.98	0.73
Ti	0.43	0.40	0.41	0.55	0.32	0.57	0.55	0.54	0.46	0.32
Total	3.91	3.91	3.90	3.91	4.01	3.86	3.55	3.87	3.89	3.94

[a] Mel* = ^{16}O-rich melilite.
[b] Mel = ^{16}O-poor melilite.

of melilite has a relatively ^{16}O-poor composition: Δ^{17}O values of these melilites range from −9‰ to −3‰ (Table 6). The Δ^{17}O values of melilite in the rim are from −19‰ to −13‰ (Table 6).

3.3.2. *Fassaite*

3.3.2.1. 7R-19-1(a). The Δ^{17}O values of the angular fassaite range from −15‰ to +1‰ (Table 7). The Δ^{17}O value of a small fassaite inclusion (20 μm in diameter) in the Mel crystal is −8‰. The Δ^{17}O values of a small fassaite inclusion in the Mel* crystal ranges from −19 to −15‰, i.e., it appears to have the same O isotopic composition as the surrounding ^{16}O-rich

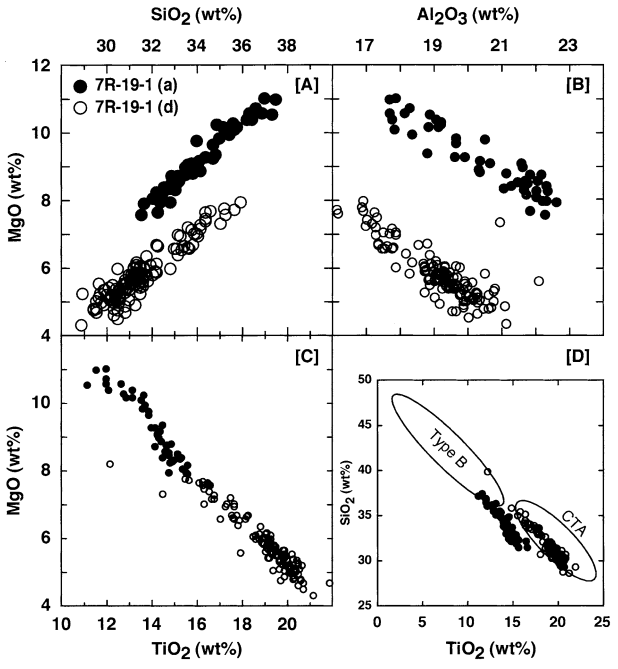

Fig. 6. Oxide relationship of fassaite in 7R-19-1(a) and in 7R-19-1(d). Solid and open circles are measured points in 7R-19-1(a) and in 7R-19-1(d), respectively. [a] MgO vs. SiO_2, [b] MgO vs. Al_2O_3, [c] MgO vs. TiO_2, and [d] SiO_2 vs. TiO_2. Two ellipses shown in [d] are typical ranges of Type B and compact Type A inclusions (Simon et al., 1999).

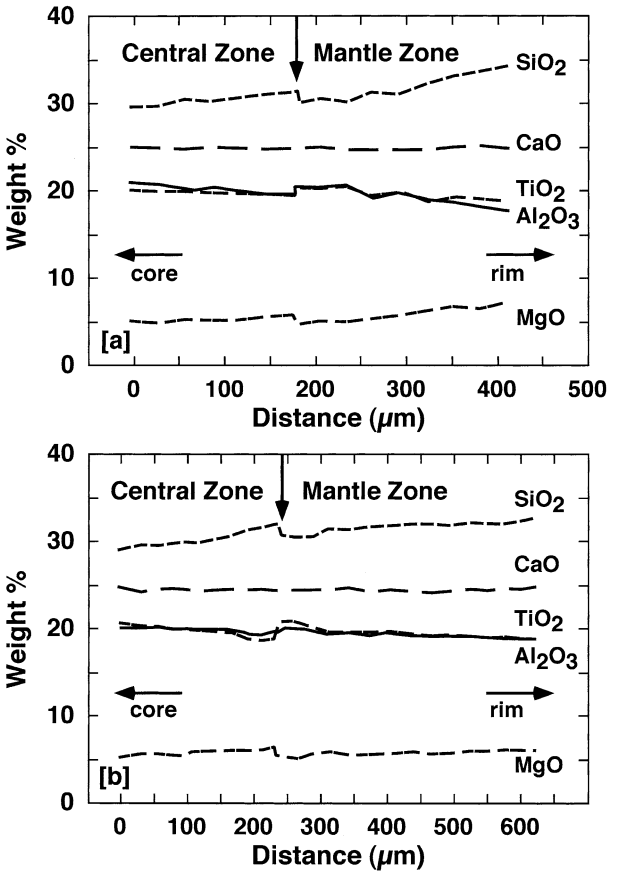

Fig. 7. Results of SEM-EDS traverse analysis across the angular fassaite in 7R-19-1(d). Oxide abundance is plotted against distance from core to rim for line profile 1 [a] and line profile 2 [b] of Figure 2.

Table 4. Representative analysis of spinel in 7R-19-1 (d) (wt%).

	Blocky				Irregular in center				Irregular in rim			
	1	2	3	4	1	2	3	4	1	2	3	4
MgO	30.3	29.6	29.9	29.6	26.7	26.6	25.7	27.0	29.2	25.3	27.5	26.4
Al_2O_3	69.7	69.6	69.4	69.4	69.8	68.2	67.3	68.9	69.0	67.0	61.3	62.8
CaO	nd[a]	0.8	nd	1.0	nd	1.3	1.7	0.5	nd	1.8	4.0	4.6
TiO_2	nd	nd	0.7	nd	nd	0.8	1.9	nd	nd	nd	5.3	6.2
FeO	nd	nd	nd	nd	3.5	3.1	3.4	3.6	1.9	5.9	1.9	nd
Total	100	100	100	100	100	100	100	100	100	100	100	100
	Cations per 4 oxygen anions											
Mg	1.07	1.05	1.06	1.06	0.96	0.96	0.93	0.97	1.04	0.92	1.00	0.98
Al	1.95	1.95	1.94	1.96	1.98	1.94	1.93	1.96	1.94	1.92	1.77	1.80
Ca	nd	0.02	nd	0.01	nd	0.03	0.04	0.01	nd	0.05	0.10	0.12
Ti	nd	nd	0.01	nd	nd	0.02	0.03	nd	nd	nd	0.10	0.11
Fe	nd	nd	nd	nd	0.07	0.06	0.07	0.07	0.03	0.11	0.03	nd
Total	3.02	3.02	3.01	3.03	3.01	3.01	3.00	3.01	3.01	3.00	3.00	3.01

[a] nd = not detected.

Mel* crystal (Table 7). The O isotopic composition of the small fassaite inclusion in the Mel crystal is depleted in ^{16}O compared to the small fassaite in Mel*, but slightly enriched compared to the surrounding ^{16}O-poor Mel crystal (Table 7). The wide variation in O isotopic composition of fassaite crystals indicates that the crystallization of fassaite in 7R-19-1 continued from ^{16}O-rich to ^{16}O-poor melts.

3.3.2.2. 7R-19-1(d). The $\Delta^{17}O$ values of the large angular fassaite crystal range from −15‰ to +1‰ (Fig. 8 and Table 7). The $\Delta^{17}O$ values of the small, rectangular fassaite crystal range from −5‰ to −3‰ (Fig. 2 [a] and Table 7). The distributions of O isotopic composition of fassaite in 7R-19-1(d) are similar to those of fassaite in 7R-19-1(a). The $\Delta^{17}O$ value of a small rectangular fassaite (20 × 10 μm) in a spinel grain is −16‰ (Table 7), which is similar to that in surrounding spinel (Table 8). This fassaite grain appears to have the same O isotopic composition as the surrounding ^{16}O-rich spinel, suggesting an inclusion of the spinel grain.

We have measured line profiles of O isotopes within the large single crystal of fassaite across the growth zone (Fig. 2). The O isotopic measurements for line profiles consist of 13 points at intervals of ~32 μm (Fig. 11 [a]), and of 19 points at the intervals of ~35 μm (Fig. 11). The $\Delta^{17}O$ distributions of line profile 01 and 02 in the angular fassaite range from −14‰ to −8‰ and from −13‰ to −4‰, respectively (Table 7). Both line profiles show relatively homogeneous distributions of ^{16}O enrichment within the analytical error (Fig. 11). We did not find any evidence for systematic exchanges of O isotopic distributions during the fassaite crystallization.

3.3.3. Spinel

3.3.3.1. 7R-19-1(a). The $\Delta^{17}O$ values of spinel range from −21‰ to −16‰ (Table 8). All spinel grains have the same large negative $\Delta^{17}O$ of ~ −20‰ within the analytical error (~ ±5‰).

Table 5. Representative analysis of minor minerals in 7R-19-1(d) (wt%).

	Hibonite			Anorthite			Perovskite		
	1	2	3	1	2	3	1	2	3
NaO	nd[a]	nd	nd	nd	nd	1.2	nd	nd	nd
MgO	5.5	4.0	4.6	nd	nd	nd	nd	1.0	0.2
Al_2O_3	84.2	79.9	82.2	42.0	39.0	52.1	2.5	5.6	1.7
SiO_2	nd	1.8	nd	41.0	42.6	32.3	3.0	nd	nd
CaO	5.9	8.4	7.3	17.0	18.4	14.5	41.2	39.5	41.1
TiO_2	4.4	6.1	5.9	nd	nd	nd	53.3	53.9	57.0
Total	100	100	100	100	100	100	100	100	100
	Cations per 19 oxygen anions			Cations per 8 oxygen anions			Cations per 3 oxygen anions		
Na	nd	nd	nd	nd	nd	0.04	nd	nd	nd
Mg	0.92	0.65	0.78	nd	nd	nd	nd	0.03	0.01
Al	11.09	10.61	10.89	2.27	2.12	2.82	0.06	0.15	0.05
Si	nd	0.20	nd	1.88	1.96	1.49	0.07	nd	nd
Ca	0.71	1.01	0.88	0.84	0.9	0.71	0.98	0.94	0.99
Ti	0.37	0.52	0.50	nd	nd	nd	0.89	0.9	0.97
Total	13.09	12.99	13.05	4.99	4.98	5.06	2.00	2.02	2.02
AN				100	100	95			

[a] nd = not detected.

Table 6. Oxygen isotopic compositions of melilite in 7R-19-1.

Analysis	$\delta^{17}O_{SMOW}$ (‰)	$\delta^{18}O_{SMOW}$ (‰)	$\Delta^{17}O_{SMOW}$[a] (‰)
7R-19-1 (a)			
Mel (^{16}O-poor melilite)			
a_M-10	−4.1 ± 3.5	−9.8 ± 1.8	1.0 ± 3.9
a_M-11	−4.6 ± 3.6	−12.7 ± 2.1	2.0 ± 3.8
a_M-12	−13.4 ± 3.1	−9.6 ± 2.1	−8.4 ± 3.8
a_M-15	−10.4 ± 3.2	−8.1 ± 2.1	−6.2 ± 3.8
a_M-38	−11.1 ± 3.4	−10.3 ± 2.1	−5.7 ± 4.0
a_M-39	−10.8 ± 3.5	−8.3 ± 1.9	−6.4 ± 4.0
Mel* (^{16}O-rich melilite)			
a_M-01	−28.8 ± 3.4	−30.2 ± 2.0	−13.1 ± 4.0
a_M-02	−29.8 ± 2.7	−24.6 ± 1.9	−17.1 ± 3.3
a_M-03	−33.0 ± 3.0	−34.0 ± 2.0	−15.3 ± 3.6
a_M-04	−31.3 ± 3.0	−32.9 ± 2.0	−14.1 ± 3.6
a_M-05	−32.9 ± 2.6	−34.7 ± 2.0	−14.8 ± 3.3
a_M-06	−38.0 ± 3.0	−34.9 ± 2.0	−19.8 ± 3.6
a_M-07	−37.7 ± 3.2	−28.9 ± 2.2	−22.7 ± 3.9
a_M-08	−42.3 ± 3.1	−33.6 ± 2.1	−24.8 ± 3.8
a_M-09	−29.0 ± 2.8	−31.7 ± 2.1	−12.6 ± 3.5
a_M-14	−40.3 ± 3.0	−43.9 ± 1.9	−17.5 ± 3.5
a_M-30	−48.0 ± 2.9	−43.8 ± 1.7	−25.2 ± 3.3
a_M-37	−38.8 ± 3.0	−40.2 ± 1.5	−17.9 ± 3.4
a_M-41	−32.3 ± 3.4	−34.2 ± 2.4	−14.5 ± 4.2
a_M-54	−43.4 ± 3.0	−35.1 ± 2.3	−25.1 ± 3.8
a_M-55	−44.3 ± 3.0	−39.7 ± 1.4	−23.6 ± 3.3
a_M-56	−43.9 ± 2.7	−42.4 ± 1.6	−21.9 ± 3.2
a_M-57	−39.5 ± 2.8	−44.4 ± 1.5	−16.4 ± 3.2
a_M-58	−36.4 ± 2.9	−43.8 ± 1.7	−13.6 ± 3.3
a_M-59	−38.0 ± 3.0	−43.1 ± 1.4	−15.6 ± 3.3
Line profile between Mel & Mel*			
a_M-16	−39.8 ± 3.0	−36.1 ± 1.9	−21.1 ± 3.6
a_M-21	−18.4 ± 3.2	−12.5 ± 2.2	−11.9 ± 3.8
a_M-45	−36.1 ± 2.9	−36.3 ± 1.5	−17.1 ± 3.2
a_M-47	−10.0 ± 3.0	−8.9 ± 1.6	−5.4 ± 3.4
a_M-48	−22.1 ± 3.2	−20.5 ± 1.8	−11.5 ± 3.6
a_M-49	−35.5 ± 3.4	−38.7 ± 1.8	−15.3 ± 3.8
a_M-50	−27.9 ± 3.1	−33.0 ± 1.6	−10.7 ± 3.5
a_M-51	−9.7 ± 3.2	−13.7 ± 1.8	−2.6 ± 3.6
a_M-52	−18.1 ± 3.1	−9.2 ± 1.8	−13.3 ± 3.6
a_M-53	−12.5 ± 2.9	−11.5 ± 1.9	−6.5 ± 3.5
Line profile within Mel*			
a_M-31	−23.0 ± 3.0	−21.3 ± 1.7	−11.9 ± 3.4
a_M-32	−19.5 ± 3.2	−11.1 ± 1.4	−13.7 ± 3.5
a_M-33	−14.1 ± 3.0	−11.8 ± 1.6	−7.9 ± 3.4
a_M-34	−35.0 ± 2.9	−33.8 ± 1.6	−17.4 ± 3.3
a_M-35	−36.7 ± 3.0	−33.6 ± 1.6	−19.3 ± 3.4
a_M-36	−10.1 ± 2.7	−5.8 ± 1.6	−7.1 ± 3.2
7R-19-1 (d)			
d_M-01	−7.6 ± 2.8	−5.7 ± 1.5	−4.6 ± 3.2
d_M-04	−2.2 ± 3.3	−2.9 ± 1.5	−0.7 ± 3.6
d_M-05	−7.4 ± 3.2	−2.1 ± 1.6	−6.3 ± 3.6
d_M-06	4.3 ± 3.0	4.1 ± 1.7	2.1 ± 3.5
d_M-07	−0.7 ± 3.3	1.6 ± 1.8	−1.5 ± 3.8
d_M-10	−2.5 ± 3.5	0.0 ± 1.7	−2.5 ± 3.9
d_M-11	−10.3 ± 2.8	−6.4 ± 1.5	−6.9 ± 3.1
d_M-12	−13.9 ± 2.8	−10.8 ± 1.5	−8.3 ± 3.3
d_M-13	−33.0 ± 3.3	−26.6 ± 1.6	−19.2 ± 3.4
d_M-14	−4.9 ± 3.3	−1.6 ± 1.6	−4.1 ± 3.7
d_M-15	−28.9 ± 3.0	−19.7 ± 1.5	−18.6 ± 3.4
d_M-16	−11.0 ± 3.2	−1.2 ± 1.5	−10.4 ± 3.6
d_M-17	−17.5 ± 2.8	−4.8 ± 1.8	−15.0 ± 3.3
d_M-18	0.5 ± 3.5	1.9 ± 1.7	−0.5 ± 3.9
d_M-19	−24.6 ± 3.0	−16.2 ± 1.9	−16.1 ± 3.6
d_M-20	−16.6 ± 2.7	−5.8 ± 1.5	−13.5 ± 3.1
d_M-21	−19.0 ± 3.4	−14.6 ± 1.6	−11.4 ± 3.8
d_M-22	−18.2 ± 3.5	−13.1 ± 1.8	−11.4 ± 3.9

Table 6. (Continued)

Analysis	$\delta^{17}O_{SMOW}$ (‰)	$\delta^{18}O_{SMOW}$ (‰)	$\Delta^{17}O_{SMOW}$[a] (‰)
7R-19-1 (d)			
d_M-25	−15.8 ± 3.2	−16.1 ± 1.8	−7.4 ± 3.7
d_M-29	−2.8 ± 3.5	−1.0 ± 1.7	−2.2 ± 3.9
d_M-35	11.8 ± 3.1	13.2 ± 1.6	4.9 ± 3.5
d_M-36	9.2 ± 3.2	5.5 ± 2.2	6.3 ± 3.9
d_M-37	12.2 ± 3.3	11.1 ± 1.8	6.4 ± 3.8
d_M-38	14.3 ± 3.4	13.5 ± 1.8	7.3 ± 3.8
d_M-39	7.2 ± 3.2	14.6 ± 1.9	−0.4 ± 3.8
d_M-40	10.9 ± 2.9	15.9 ± 1.8	2.6 ± 3.4
d_M-42	−18.8 ± 3.3	−14.7 ± 1.5	−11.2 ± 3.6
d_M-43	−19.5 ± 3.0	−19.1 ± 1.6	−9.6 ± 3.4
d_M-44	−18.0 ± 2.6	−22.0 ± 1.4	−6.5 ± 2.9
d_M-45	−22.0 ± 3.1	−11.8 ± 1.7	−15.9 ± 3.5
d_M-46	2.3 ± 3.1	5.9 ± 1.7	−0.7 ± 3.6
d_M-47	4.5 ± 2.9	5.7 ± 1.7	1.5 ± 3.4
d_M-48	0.1 ± 3.2	9.1 ± 1.6	−4.6 ± 3.6
d_M-49	−5.9 ± 2.7	−0.8 ± 1.7	−5.4 ± 3.2
d_M-50	−18.8 ± 2.8	−16.0 ± 1.7	−10.5 ± 3.3
d_M-51	−6.6 ± 3.2	−13.8 ± 1.5	0.6 ± 3.5
d_M-52	−21.4 ± 3.5	−17.9 ± 1.7	−12.1 ± 3.9
d_M-53	−11.2 ± 2.9	−9.0 ± 1.7	−6.5 ± 3.3
d_M-54	−31.6 ± 3.0	−28.5 ± 1.5	−16.8 ± 3.3
d_M-55	−5.1 ± 2.8	−5.0 ± 1.5	−2.5 ± 3.2
d_M-56	4.9 ± 2.9	2.8 ± 1.6	3.5 ± 3.3
d_M-57	1.6 ± 3.4	8.1 ± 1.7	−2.6 ± 3.8
d_M-63	3.5 ± 3.0	14.7 ± 1.8	−4.2 ± 3.5
d_M-64	10.3 ± 2.9	18.3 ± 1.7	0.8 ± 3.3
d_M-65	11.0 ± 3.0	17.8 ± 1.6	1.7 ± 3.4
d_M-66	−16.4 ± 2.4	−7.9 ± 1.7	−12.3 ± 3.0
d_M-69	−22.7 ± 3.1	−9.3 ± 1.9	−17.8 ± 3.7
d_M-72	−24.4 ± 2.8	−13.7 ± 1.6	−17.2 ± 3.2
d_M-73	6.6 ± 3.3	5.0 ± 1.8	4.0 ± 3.8
d_M-74	−15.4 ± 3.1	−16.2 ± 1.5	−7.0 ± 3.4
d_M-75	−23.6 ± 2.9	−22.2 ± 1.7	−12.1 ± 3.3
d_M-76	−20.8 ± 3.0	−20.6 ± 1.6	−10.0 ± 3.4
d_M-77	0.6 ± 2.4	8.2 ± 1.5	−3.6 ± 2.8
d_M-78	0.0 ± 3.0	8.8 ± 1.7	−4.5 ± 3.4
d_M-79	−1.1 ± 3.1	−1.7 ± 1.4	−0.2 ± 3.4
d_M-80	−21.1 ± 3.2	−19.3 ± 1.5	−11.1 ± 3.5
d_M-81	−9.2 ± 2.8	−11.2 ± 1.5	−3.4 ± 3.2
d_M-82	−0.7 ± 3.1	0.8 ± 1.7	−1.1 ± 3.5
g#1			
d_M-02	−6.5 ± 3.0	2.5 ± 1.5	−7.8 ± 3.4
d_M-03	−1.5 ± 3.0	5.2 ± 1.7	−4.3 ± 3.4
g#2			
d_M-08	−3.9 ± 3.3	2.5 ± 1.8	−5.2 ± 3.7
d_M-09	−4.1 ± 3.1	−3.2 ± 1.6	−2.5 ± 3.5
d_M-41	0.6 ± 3.2	7.3 ± 1.6	−3.2 ± 3.6
d_M-62	1.7 ± 3.5	1.5 ± 1.6	0.9 ± 3.8
d_M-83	−6.3 ± 2.2	−7.4 ± 3.7	−4.3 ± 3.4
g#3			
d_M-23	−27.8 ± 2.8	−28.4 ± 1.7	−13.0 ± 3.3
d_M-24	−34.6 ± 3.4	−30.0 ± 1.8	−19.0 ± 3.9
Center			
d_M-26	1.5 ± 3.5	1.5 ± 1.7	0.8 ± 3.9
d_M-27	5.1 ± 2.7	4.9 ± 1.4	2.5 ± 3.1
d_M-28	−3.5 ± 3.3	0.6 ± 1.8	−3.8 ± 3.8
d_M-58	−16.3 ± 3.1	−14.9 ± 1.8	−8.6 ± 3.6
d_M-59	−2.2 ± 3.5	0.6 ± 1.9	−2.5 ± 4.0
d_M-60	−13.4 ± 2.8	−13.1 ± 1.8	−6.6 ± 3.3
d_M-61	−6.0 ± 3.2	−0.4 ± 1.8	−5.8 ± 3.7
d_M-67	−10.4 ± 3.1	−7.6 ± 1.6	−6.4 ± 3.5
Rim			
d_M-68	−3.5 ± 3.3	5.0 ± 1.6	−6.1 ± 3.7
d_M-70	−14.5 ± 3.4	−6.4 ± 1.8	−11.2 ± 3.9
d_M-71	−17.4 ± 3.3	−15.2 ± 1.7	−9.5 ± 3.7

Table 6. (Continued)

Analysis	$\delta^{17}O_{SMOW}$ (‰)	$\delta^{18}O_{SMOW}$ (‰)	$\Delta^{17}O_{SMOW}$[a] (‰)
7R-19-1 (e)			
		^{16}O-poor melilite	
e_M-15	−8.6 ± 3.3	9.9 ± 1.6	−3.7 ± 3.7
e_M-16	−12.7 ± 3.0	−6.6 ± 1.7	−9.3 ± 3.4
e_M-17	−12.3 ± 2.9	−17.8 ± 1.6	−3.1 ± 3.3
		^{16}O-rich melilite	
e_M-01	−26.2 ± 3.1	−19.3 ± 1.5	−16.2 ± 3.5
e_M-02	−35.2 ± 2.9	−37.1 ± 1.7	−15.8 ± 3.4
e_M-03	−25.0 ± 2.8	−29.9 ± 1.6	−9.5 ± 3.2
e_M-04	−42.2 ± 2.9	−43.9 ± 1.3	−19.3 ± 3.2
e_M-05	−24.8 ± 3.0	−25.0 ± 1.6	−11.8 ± 3.4
e_M-06	−33.7 ± 2.7	−33.7 ± 1.7	−14.2 ± 3.2
e_M-07	−29.7 ± 3.0	−32.5 ± 1.6	−12.8 ± 3.4
e_M-08	−25.7 ± 2.8	−26.7 ± 2.0	−11.8 ± 3.4
e_M-09	−28.4 ± 3.1	−27.8 ± 1.7	−13.9 ± 3.6
e_M-10	−29.8 ± 3.6	−31.0 ± 1.5	−13.7 ± 3.9
e_M-11	−29.5 ± 3.5	−28.3 ± 1.6	−14.8 ± 3.8
e_M-12	−33.7 ± 3.0	−36.3 ± 1.6	−14.8 ± 3.4
e_M-13	−42.8 ± 2.7	−49.8 ± 1.4	−16.9 ± 3.0
e_M-14	−41.4 ± 3.0	−42.0 ± 1.5	−19.5 ± 3.3
e_M-18	−35.8 ± 3.2	−31.7 ± 1.6	−19.3 ± 3.6
e_M-20	−40.8 ± 2.7	−42.5 ± 1.5	−18.7 ± 3.1
e_M-21	−21.9 ± 3.0	−15.3 ± 1.6	−13.9 ± 3.4
		Rim	
e_M-22	−19.7 ± 2.9	−12.8 ± 1.9	−13.0 ± 3.5
e_M-23	−29.5 ± 3.1	−19.8 ± 1.6	−19.2 ± 3.5

[a] $\Delta^{17}O = \delta^{17}O - 0.52 \times \delta^{18}O$. Errors are calculated from error propagation of $\delta^{17}O$ and $\delta^{18}O$.

3.3.3.2. 7R-19-1(d). The $\Delta^{17}O$ values of spinel range from −29‰ to −14‰. The blocky spinel crystal included in a small fassaite grain was ^{16}O-rich ($\Delta^{17}O = -29‰$). The spinel crystal in the central area near the small perovskite crystals is also ^{16}O-rich ($\Delta^{17}O = -26‰$), as is an irregular spinel in the rim adjacent to a melilite crystal ($\Delta^{17}O = -20‰$) (Table 8).

3.3.3.3. 7R-19-1(e). The $\Delta^{17}O$ values of spinel range from −26‰ to −17‰. The $\Delta^{17}O$ value of the spinel near the small fine-grained perovskite in the rim is −21‰ (Table 8).

3.3.4. Accessory minerals (hibonite and perovskite)

In 7R-19-1(d), the hibonite in the central area surrounding irregular-shaped melilite was enriched in ^{16}O ($\Delta^{17}O = \sim -23‰$) (Fig. 2 and Table 9). The small perovskite surrounding the irregularly shaped spinel crystal, irregularly shaped aggregate of melilite and alteration products in the center area was ^{16}O-poor ($\Delta^{17}O = -7‰$) (Table 9).

In 7R-19-1(e), the $\Delta^{17}O$ value of fine-grained perovskite in the rim surrounding spinel and the alteration products anorthite, Fe-rich spinel and altered melilite, was −11‰ (Table 9).

4. DISCUSSION

4.1. Chemical Composition of 7R-19-1

The bulk chemical composition estimated from the analysis of 7R-19-1 falls near the area for Type A CAIs in the anorthite-gehlenite-forsterite system (Fig. 4), and hence, based on chemical composition, 7R-19-1 may be classified as fassaite-rich, compact Type A CAI. Chemical analysis of melilite indicates a peak at $Åk_{15–20}$ in the abundance-composition histogram (Fig. 5), which also corresponds to Type A. Although, from modal compositions of melilite, fassaite and spinel, this inclusion might be designated as Type B, small amounts of fassaite are often observed in coarse-grained Type A inclusions. Therefore, from combined textural, mineral and the bulk chemical compositions, 7R-19-1 can be designated as a coarse-grained compact Type A with a mostly volatile chemical composition.

The large angular fassaite in 7R-19-1(d) (Fig. 2) is compositionally zoned from core to rim. MgO, SiO_2, Al_2O_3 and TiO_2 concentrations abruptly change at the boundary between the central and mantle zones (Fig. 7). The zones appear to be the product of growth zoning from liquid based on the observed change (Fig. 7). The trends of MgO, SiO_2, Al_2O_3 and TiO_2 zoning in the central zone are not different, however, from those in the mantle zone. Thus, mantle zones probably represent overgrowths on the central zone. The trends in the central zone indicate that Al_2O_3 and TiO_2-rich contents in the melt gradually decreased with crystallization. A sharp boundary of the zoning profiles of MgO, SiO_2, Al_2O_3 and TiO_2 indicates that the liquid compositions changed before the starting of mantle-zone crystallization. The curved and irregular boundary suggests that melting of the central zone occurred before mantle crystallization.

4.2. O Isotopic Compositions in 7R-19-1

In 7R-19-1, three major refractory minerals (spinel, melilite and fassaite) show large negative $\Delta^{17}O$ anomalies decreasing in the order, spinel ∼ melilite > fassaite (Fig. 8). The order of the O isotope anomalies normally observed for coarse-grained CAIs, on the other hand, is spinel > fassaite > melilite. In this respect, 7R-19-1 is unusual. Experimental investigation of the crystallization sequence from Ca, Al-rich liquid (Stolper, 1982; Stolper and Paque 1986) showed that spinel was the first mineral to crystallize, followed by melilite. If crystallization of the CAI started from an ^{16}O-rich liquid, the first crystallized minerals including melilite would have an ^{16}O-rich composition. Except for the existence of ^{16}O-poor melilite in 7R-19-1, the order of the O isotopic anomaly of the three major refractory minerals is consistent with this crystallization sequence. If crystallization of the CAI started from an ^{16}O-rich liquid in ^{16}O-poor gas such as in the dynamic exchange model of Ryerson and McKeegan (1994), gradual zoning of O isotopes is expected in melilite. However, the sharp boundary between ^{16}O-rich and ^{16}O-poor regions in melilite is not consistent with this model. Various O isotopic compositions in fassaite crystals in 7R-19-1 also argue against the model; for fassaite, this difficulty has already been pointed out by Ryerson and McKeegan (1994). Therefore, ^{16}O-poor melilite may have crystallized at a later stage during ^{16}O-poor conditions without significant influence of diffusion.

The order of the O isotope anomalies in 7R-19-1 and that in coarse-grained CAIs reported previously are different; however, the lower limit values for $\delta^{17,\ 18}O/^{16}O$ (about −21‰ in $\Delta^{17}O$) are similar (Fig. 8). The same lower value also has been observed in CAIs of ordinary and other meteorite groups (Clayton, 1993). In recent SIMS studies (Fahey et al., 1987; McKeegan, 1987; Zinner et al., 1991; Yurimoto et al., 1994, 1998;

Table 7. Oxygen isotopic compositions of fassaite in 7R-19-1.

Analysis	$\delta^{17}O_{SMOW}$ (‰)	$\delta^{18}O_{SMOW}$ (‰)	$\Delta^{17}O_{SMOW}$[c] (‰)
7R-19-1 (a)			
Angular			
a_F-01	−9.3 ± 2.8	−9.6 ± 2.1	−4.3 ± 3.5
a_F-02	−5.2 ± 2.9	−12.6 ± 2.0	1.3 ± 3.5
a_F-03	−17.2 ± 2.7	−22.4 ± 2.2	−5.5 ± 3.5
a_F-04	−3.3 ± 3.1	−8.1 ± 2.0	0.9 ± 3.7
a_F-05	−24.3 ± 3.0	−18.5 ± 2.1	−14.7 ± 3.7
a_F-06	−17.1 ± 3.4	−11.7 ± 2.1	−11.1 ± 4.0
a_F-07	−21.4 ± 3.4	−21.8 ± 2.1	−10.1 ± 4.0
a_F-08	−5.5 ± 2.5	−2.3 ± 2.1	−4.3 ± 3.3
a_F-09	0.2 ± 3.0	−1.3 ± 2.0	0.9 ± 3.7
a_F-10	1.1 ± 3.1	0.0 ± 2.1	1.2 ± 3.7
Small grain in Mel[a]			
a_F-13	−16.9 ± 3.3	−16.5 ± 2.1	−8.3 ± 3.9
Small grain in Mel*[b]			
a_F-11	−32.2 ± 3.1	−33.6 ± 2.0	−14.7 ± 3.7
a_F-12	−37.8 ± 3.0	−36.3 ± 2.0	−18.9 ± 3.6
7R-19-1 (d)			
Large angular			
d_F-02	−17.6 ± 3.2	−9.8 ± 1.7	−12.5 ± 3.6
d_F-03	−6.5 ± 3.4	−1.2 ± 1.7	−5.9 ± 3.8
d_F-04	−17.3 ± 2.9	−19.4 ± 1.9	−7.1 ± 3.4
d_F-05	−15.5 ± 3.3	−11.3 ± 1.6	−9.7 ± 3.7
d_F-06	−10.7 ± 3.0	−11.2 ± 1.5	−4.9 ± 3.3
d_F-07	−20.7 ± 3.1	−11.2 ± 1.4	−14.9 ± 3.4
d_F-10	−21.5 ± 3.2	−23.8 ± 1.6	−9.1 ± 3.6
d_F-11	−25.2 ± 3.0	−24.8 ± 1.6	−12.3 ± 3.4
d_F-12	−24.9 ± 3.0	−24.7 ± 1.5	−12.1 ± 3.3
d_F-13	−21.2 ± 3.4	−26.5 ± 1.4	−7.5 ± 3.7
d_F-14	−16.8 ± 3.0	−21.0 ± 1.4	−5.8 ± 3.3
d_F-15	−25.9 ± 2.7	−27.6 ± 1.8	−11.6 ± 3.2
d_F-16	−24.8 ± 3.2	−20.8 ± 1.6	−13.9 ± 3.5
d_F-17	−16.2 ± 2.9	−25.7 ± 1.5	−2.9 ± 3.3
d_F-18	−27.1 ± 3.5	−24.2 ± 1.6	−14.5 ± 3.9
d_F-19	−17.8 ± 3.3	−18.4 ± 1.6	−8.2 ± 3.6
d_F-20	−24.8 ± 3.3	−18.4 ± 2.2	−15.2 ± 4.0
d_F-21	−21.7 ± 2.8	−22.8 ± 1.7	−9.8 ± 3.3
d_F-42	−20.6 ± 3.3	−15.9 ± 1.6	−12.3 ± 3.7
d_F-43	−19.2 ± 2.7	−17.4 ± 1.4	−10.2 ± 3.1
d_F-44	−14.1 ± 3.0	−21.5 ± 1.7	−3.0 ± 3.4
d_F-45	−20.6 ± 2.9	−18.5 ± 1.5	−11.0 ± 3.2
d_F-46	−14.6 ± 3.2	−16.6 ± 1.6	−6.0 ± 3.6
d_F-47	−14.6 ± 3.4	−16.0 ± 1.5	−6.3 ± 3.7
d_F-48	−14.5 ± 2.8	−18.3 ± 1.5	−5.0 ± 3.2
d_F-49	−6.8 ± 3.1	−7.9 ± 1.5	−2.7 ± 3.4
d_F-50	−7.2 ± 3.3	8.7 ± 1.7	−2.7 ± 3.7
d_F-51	−2.4 ± 2.9	−7.0 ± 1.4	1.2 ± 3.2
d_F-52	−4.6 ± 2.9	4.6 ± 1.6	−7.0 ± 3.3
d_F-53	−4.7 ± 2.8	−0.3 ± 1.5	−4.6 ± 3.2
d_F-54	−11.8 ± 2.9	−5.9 ± 1.5	−8.7 ± 3.3
d_F-55	−13.5 ± 3.4	−9.2 ± 1.5	−8.7 ± 3.7
d_F-56	−17.1 ± 3.0	−13.6 ± 1.5	−10.0 ± 3.3
d_F-57	−23.2 ± 3.1	−19.2 ± 1.6	−13.2 ± 3.4
d_F-58	−21.8 ± 2.8	−19.3 ± 1.5	−11.8 ± 3.2
d_F-59	−19.5 ± 3.0	−20.2 ± 1.6	−9.0 ± 3.5
d_F-60	−15.3 ± 3.1	−19.5 ± 1.5	−5.1 ± 3.4
d_F-61	−16.5 ± 2.9	−17.0 ± 1.6	−7.6 ± 3.3
d_F-91	−3.9 ± 3.3	9.3 ± 1.5	−8.7 ± 3.7
d_F-92	−3.3 ± 2.7	9.9 ± 1.7	−8.5 ± 3.2
d_F-93	0.8 ± 2.9	10.9 ± 1.4	−4.8 ± 3.2
d_F-94	−18.5 ± 2.9	−14.8 ± 1.6	−10.8 ± 3.3
d_F-95	−16.3 ± 3.1	−9.6 ± 1.6	−11.3 ± 3.5
d_F-96	−13.0 ± 3.4	−16.6 ± 1.6	−4.4 ± 3.8
d_F-97	−18.7 ± 3.1	−11.6 ± 1.6	−12.7 ± 3.5
d_F-98	−9.8 ± 2.9	−10.1 ± 1.6	−4.5 ± 3.3
d_F-99	−18.1 ± 2.8	−11.0 ± 1.4	−12.4 ± 3.2
d_F-100	−8.0 ± 3.6	−10.6 ± 1.7	−2.5 ± 3.9
d_F-101	−12.8 ± 2.8	−14.0 ± 1.6	−5.5 ± 3.2
d_F-102	−9.7 ± 3.0	−4.2 ± 1.7	−7.5 ± 3.4
d_F-103	0.0 ± 3.0	3.2 ± 1.6	−1.7 ± 3.4
d_F-104	−0.9 ± 2.9	−2.9 ± 1.7	0.6 ± 3.3
d_F-105	−11.4 ± 3.3	−10.5 ± 1.5	−5.9 ± 3.7
d_F-106	−0.3 ± 3.2	0.7 ± 1.6	−0.7 ± 3.5
d_F-107	−7.4 ± 2.6	−3.4 ± 1.7	−5.7 ± 3.2
d_F-108	−8.5 ± 3.0	−3.6 ± 1.8	−6.7 ± 3.5
d_F-109	−17.8 ± 3.1	−15.9 ± 1.6	−9.5 ± 3.5
d_F-110	−7.1 ± 3.1	−5.5 ± 1.5	−4.3 ± 3.4
d_F-111	−8.7 ± 3.0	−8.0 ± 1.7	−4.6 ± 3.4
d_F-112	−1.7 ± 3.9	4.9 ± 1.7	−4.2 ± 3.2
d_F-113	−3.9 ± 2.5	8.4 ± 1.6	−8.3 ± 3.0
d_F-114	−12.5 ± 2.9	−2.4 ± 1.1	−11.3 ± 3.1
d_F-115	−12.5 ± 2.6	−1.4 ± 1.5	−11.8 ± 3.0
d_F-116	−2.1 ± 3.2	2.1 ± 1.5	−3.2 ± 3.6
d_F-117	−1.8 ± 2.6	6.9 ± 1.5	−5.4 ± 3.0
d_F-118	−2.3 ± 3.0	7.1 ± 1.7	−6.0 ± 3.4
d_F-119	0.0 ± 3.1	9.2 ± 1.3	−4.8 ± 3.3
d_F-120	−6.4 ± 3.8	0.9 ± 1.7	−6.8 ± 4.2
d_F-121	−1.7 ± 2.8	−1.8 ± 1.5	−0.8 ± 3.2
d_F-122	−12.9 ± 2.9	−3.2 ± 1.7	−11.3 ± 3.4
d_F-123	−10.2 ± 3.2	−2.4 ± 1.3	−8.9 ± 3.5
Small rectangular			
d_F-01	−5.1 ± 2.9	−5.0 ± 1.7	−2.5 ± 3.3
d_F-08	−8.5 ± 3.0	−7.1 ± 1.3	−4.8 ± 3.3
Small fassaite in spinel (d_S-10)[d]			
d_F-09	−36.3 ± 3.0	−39.1 ± 1.4	−16.0 ± 3.4
Line profile #1			
d_F-77	−16.5 ± 3.2	−8.2 ± 1.6	−12.2 ± 3.5
d_F-78	−14.9 ± 3.1	−8.4 ± 1.8	−10.5 ± 3.5
d_F-79	−14.7 ± 2.8	−5.3 ± 1.5	−11.9 ± 3.2
d_F-80	−18.9 ± 2.8	−10.5 ± 1.5	−13.5 ± 3.2
d_F-81	−15.7 ± 3.5	−7.2 ± 1.7	−11.9 ± 3.9
d_F-82	−17.1 ± 3.2	−13.6 ± 1.7	−10.0 ± 3.6
d_F-83	−13.8 ± 2.9	−9.1 ± 1.4	−9.1 ± 3.2
d_F-84	−12.8 ± 3.2	−6.1 ± 1.7	−9.6 ± 3.6
d_F-86	−13.6 ± 2.8	−3.1 ± 1.8	−12.0 ± 3.3
d_F-87	−13.6 ± 2.9	−3.7 ± 1.4	−11.7 ± 3.3
d_F-88	−13.3 ± 2.7	−8.7 ± 1.6	−8.7 ± 3.2
d_F-89	−14.8 ± 3.3	−12.6 ± 1.4	−8.2 ± 3.6
d_F-90	−11.6 ± 3.3	−3.9 ± 1.5	−9.6 ± 3.7
Line profile #2			
d_F-22	−15.8 ± 2.8	−16.1 ± 1.6	−7.4 ± 3.2
d_F-23	−18.1 ± 3.1	−9.8 ± 1.5	−13.0 ± 3.4
d_F-24	−21.2 ± 3.3	−15.8 ± 1.5	−13.0 ± 3.6
d_F-26	−21.7 ± 2.9	−20.1 ± 1.8	−11.2 ± 3.4
d_F-27	−13.0 ± 3.5	−15.6 ± 1.6	−4.8 ± 3.8
d_F-28	−17.5 ± 3.3	−18.5 ± 1.5	−7.8 ± 3.6
d_F-29	−23.2 ± 3.3	−20.9 ± 1.9	−12.3 ± 3.8
d_F-30	−19.3 ± 2.8	−18.7 ± 1.9	−9.5 ± 3.4
d_F-31	−17.3 ± 3.0	−15.5 ± 1.7	−9.2 ± 3.5
d_F-32	−16.8 ± 3.2	−18.9 ± 1.7	−7.0 ± 3.6
d_F-33	−23.7 ± 3.8	−21.1 ± 1.5	−12.7 ± 4.1
d_F-34	−15.5 ± 3.0	−18.5 ± 1.3	−5.9 ± 3.3
d_F-35	−19.5 ± 3.4	−12.1 ± 1.6	−13.2 ± 3.8
d_F-36	−19.3 ± 3.1	−14.6 ± 1.9	−11.7 ± 3.5
d_F-37	−10.4 ± 3.0	−11.7 ± 1.7	−4.3 ± 3.5
d_F-38	−15.1 ± 2.9	−18.4 ± 1.6	−5.6 ± 3.4
d_F-39	−15.1 ± 3.1	−12.1 ± 1.5	−8.8 ± 3.4
d_F-40	−11.9 ± 3.1	−11.4 ± 1.8	−6.0 ± 3.6
d_F-41	−8.5 ± 3.0	−3.2 ± 1.7	−6.8 ± 3.5

[a] Mel = ^{16}O-poor melilite.

[b] Mel* = ^{16}O-rich melilite.

[c] $\Delta^{17}O = \delta^{17}O - 0.52 \times \delta^{18}O$. Errors are calculated from error propagation of $\delta^{17}O$ and $\delta^{18}O$.

[d] Small rectangular fassaite crystals (d_F-09) are observed in spinel grain (d_S-10). See text.

Table 8. Oxygen isotopic compositions of spinel in 7R-19-1.

Analysis	$\delta^{17}O_{SMOW}$ (‰)	$\delta^{18}O_{SMOW}$ (‰)	$\Delta^{17}O_{SMOW}$[a] (‰)
7R-19-1 (a)			
a_S-01	−41.1 ± 3.3	−39.0 ± 1.8	−20.8 ± 3.7
a_S-02	−34.3 ± 3.0	−35.3 ± 2.0	−16.0 ± 3.7
a_S-03	−37.8 ± 2.8	−35.3 ± 2.1	−19.5 ± 3.5
a_S-05	−41.0 ± 2.9	−39.5 ± 2.2	−20.5 ± 3.6
a_S-06	−38.0 ± 3.0	−40.2 ± 2.1	−17.1 ± 3.7
a_S-08	−41.5 ± 3.3	−42.1 ± 2.3	−19.7 ± 4.0
a_S-09	−38.8 ± 2.7	−41.6 ± 1.9	−17.1 ± 3.3
a_S-12	−41.4 ± 3.1	−42.8 ± 2.0	−19.1 ± 3.7
7R-19-1 (d)			
d_S-01	−46.0 ± 3.5	−43.3 ± 1.3	−23.5 ± 3.8
d_S-02	−42.3 ± 3.2	−41.6 ± 1.7	−20.7 ± 3.7
d_S-03	−32.1 ± 3.1	−34.2 ± 1.4	−14.3 ± 3.4
d_S-04	−42.1 ± 3.1	−42.2 ± 1.4	−20.1 ± 3.4
d_S-05	−41.2 ± 3.0	−39.2 ± 1.6	−20.8 ± 3.4
d_S-06	−41.8 ± 3.2	−38.6 ± 1.6	−21.8 ± 3.6
d_S-07	−39.9 ± 3.0	−36.6 ± 1.5	−20.9 ± 3.3
d_S-09	−44.6 ± 3.1	−40.9 ± 1.6	−23.3 ± 3.5
d_S-11	−37.6 ± 3.0	−43.4 ± 1.6	−15.0 ± 3.4
d_S-12	−44.2 ± 3.0	−33.3 ± 1.6	−26.9 ± 3.4
d_S-13	−43.4 ± 3.1	−43.4 ± 1.5	−20.8 ± 3.5
d_S-14	−40.6 ± 2.8	−38.3 ± 1.5	−20.6 ± 3.2
d_S-15	−42.8 ± 3.2	−41.7 ± 1.6	−21.2 ± 3.6
d_S-19	−39.9 ± 2.8	−35.3 ± 1.7	−21.6 ± 3.3
d_S-20	−38.4 ± 3.1	−40.7 ± 1.6	−17.2 ± 3.5
d_S-21	−41.6 ± 3.4	−40.2 ± 1.7	−20.7 ± 3.8
d_S-22	−41.6 ± 3.4	−43.2 ± 1.7	−24.1 ± 3.3
d_S-23	−40.4 ± 3.6	−37.9 ± 1.6	−20.7 ± 3.9
d_S-25	−46.0 ± 3.0	−41.3 ± 1.7	−24.5 ± 3.5
d_S-26	−39.2 ± 3.6	−35.9 ± 1.5	−20.5 ± 3.9
d_S-27	−40.4 ± 3.1	−36.2 ± 1.6	−21.6 ± 3.5
d_S-28	−44.9 ± 3.0	−42.7 ± 1.6	−22.7 ± 3.4
d_S-29	−40.6 ± 2.7	−42.7 ± 1.5	−18.3 ± 3.1
d_S-30	−43.4 ± 2.7	−42.5 ± 1.7	−21.3 ± 3.2
d_S-31	−41.8 ± 3.3	−42.0 ± 1.6	−19.9 ± 3.7
d_S-32	−40.1 ± 3.0	−44.6 ± 1.6	−16.9 ± 3.4
d_S-33	−39.6 ± 2.6	−41.0 ± 1.3	−18.2 ± 2.9
d_S-34	−36.7 ± 2.9	−44.3 ± 1.7	−13.7 ± 3.3
d_S-35	−48.7 ± 3.1	−38.5 ± 1.5	−28.7 ± 3.4
d_S-36	−41.0 ± 2.7	−43.3 ± 1.5	−18.4 ± 3.1
d_S-42	−43.0 ± 3.4	−38.8 ± 1.5	−22.8 ± 3.7
d_S-43	−42.5 ± 3.5	−43.4 ± 1.5	−19.9 ± 3.7
d_S-44	−35.2 ± 3.0	−36.1 ± 1.7	−16.5 ± 3.4
d_S-45	−43.2 ± 2.9	−41.9 ± 1.6	−21.4 ± 3.3
d_S-46	−44.6 ± 2.7	−39.7 ± 1.4	−23.9 ± 3.1
d_S-47	−43.1 ± 3.0	−42.6 ± 1.5	−20.9 ± 3.4
d_S-48	−39.4 ± 2.9	−39.3 ± 1.5	−19.0 ± 3.3
d_S-49	−42.6 ± 3.1	−38.1 ± 1.6	−22.8 ± 3.5
d_S-50	−43.5 ± 3.7	−38.7 ± 1.4	−23.4 ± 3.9
d_S-51	−36.8 ± 3.1	−41.0 ± 1.3	−15.4 ± 3.4
d_S-52	−44.9 ± 3.2	−40.2 ± 1.4	−23.9 ± 3.5
Spinel containing small fassaite (d_F-09)[b]			
d_S-10	−43.0 ± 3.0	−27.7 ± 1.5	−28.6 ± 3.3
Center			
d_S-08	43.7 ± 2.8	−34.7 ± 1.5	−25.7 ± 3.1
Rim			
d_S-24	43.6 ± 2.7	−45.2 ± 1.9	−20.2 ± 3.5

Table 8. (Continued)

Analysis	$\delta^{17}O_{SMOW}$ (‰)	$\delta^{18}O_{SMOW}$ (‰)	$\Delta^{17}O_{SMOW}$[a] (‰)
7R-19-1 (e)			
e_S-01	−41.9 ± 3.3	−43.5 ± 1.5	−19.3 ± 3.6
e_S-02	−45.3 ± 2.9	−36.7 ± 1.2	−26.2 ± 3.1
e_S-03	−38.7 ± 2.6	−41.8 ± 1.2	−16.9 ± 2.9
e_S-04	−41.1 ± 3.0	−41.5 ± 1.7	−19.6 ± 3.5
e_S-05	−41.8 ± 2.9	−40.8 ± 1.7	−20.6 ± 3.4
Rim			
e_S-06	−41.6 ± 2.9	−39.2 ± 1.5	−21.2 ± 3.3

[a] $\Delta^{17}O = \delta^{17}O - 0.52 \times \delta^{18}O$. Errors are calculated from error propagation of $\delta^{17}O$ and $\delta^{18}O$.

[b] Small rectangular fassaite crystals (d_F-09) are observed in spinel grain (d_S-10). See text.

McKeegan et al., 1998), an ^{16}O excess of ~ −21‰ ($\Delta^{17}O$), as also defined by conventional measurements of CAIs, is generally considered the endmember composition except for a single chondrule having an ^{16}O excess of ~ −40‰ ($\Delta^{17}O$) (Kobayashi et al., 2003). The similarity in the extreme values of ~ −21‰ ($\Delta^{17}O$) and the existence of ^{16}O-rich melilite and spinel crystals demonstrate that the crystallization of 7R-19-1 started from a liquid with an ^{16}O-rich composition of ~ −21‰ ($\Delta^{17}O$) relative to terrestrial oxygen, and supports the hypothesis that CAI precursors were originally enriched in ^{16}O. These O isotopic characteristics observed for 7R-19-1 are consistent with simple solidification of a Ca, Al-rich liquid following the experimentally determined crystallization sequence (Stolper, 1982; Stolper and Paque 1986). Thus, the CAI initially crystallized from an ^{16}O and Ca, Al-rich liquid in the early solar nebula.

4.2.1. *O isotopic composition in spinel*

All the spinel grains, including the blocky grains in 7R-19-1(a), (d) and (e) and the irregularly shaped grains in the rim of (d) and (e), are enriched in ^{16}O by about $\delta^{17,\ 18}O = -40‰$ (Fig. 8 [c]).

In 7R-19-1(a), spinel grains are scattered throughout the ^{16}O

Table 9. Oxygen isotopic compositions of minor minerals in 7R-19-1.

Analysis	$\delta^{17}O_{SMOW}$ (‰)	$\delta^{18}O_{SMOW}$ (‰)	$\Delta^{17}O_{SMOW}$[a] (‰)
7R-19-1 (d)			
Perovskite in center			
d_Pv-01	−7.9 ± 3.0	−2.2 ± 1.4	−6.7 ± 3.3
Hibonite in center			
d_Hb-01	−46.1 ± 2.8	−41.9 ± 1.5	−24.3 ± 3.2
d_Hb-02	−44.0 ± 3.1	−43.6 ± 1.5	−21.3 ± 3.5
7R-19-1 (e)			
Perovskite in rim			
e_Pv-01	−12.7 ± 2.8	−3.8 ± 1.6	−10.7 ± 3.2

[a] $\Delta^{17}O = \delta^{17}O - 0.52 \times \delta^{18}O$. Errors are calculated from error propagation of $\delta^{17}O$ and $\delta^{18}O$.

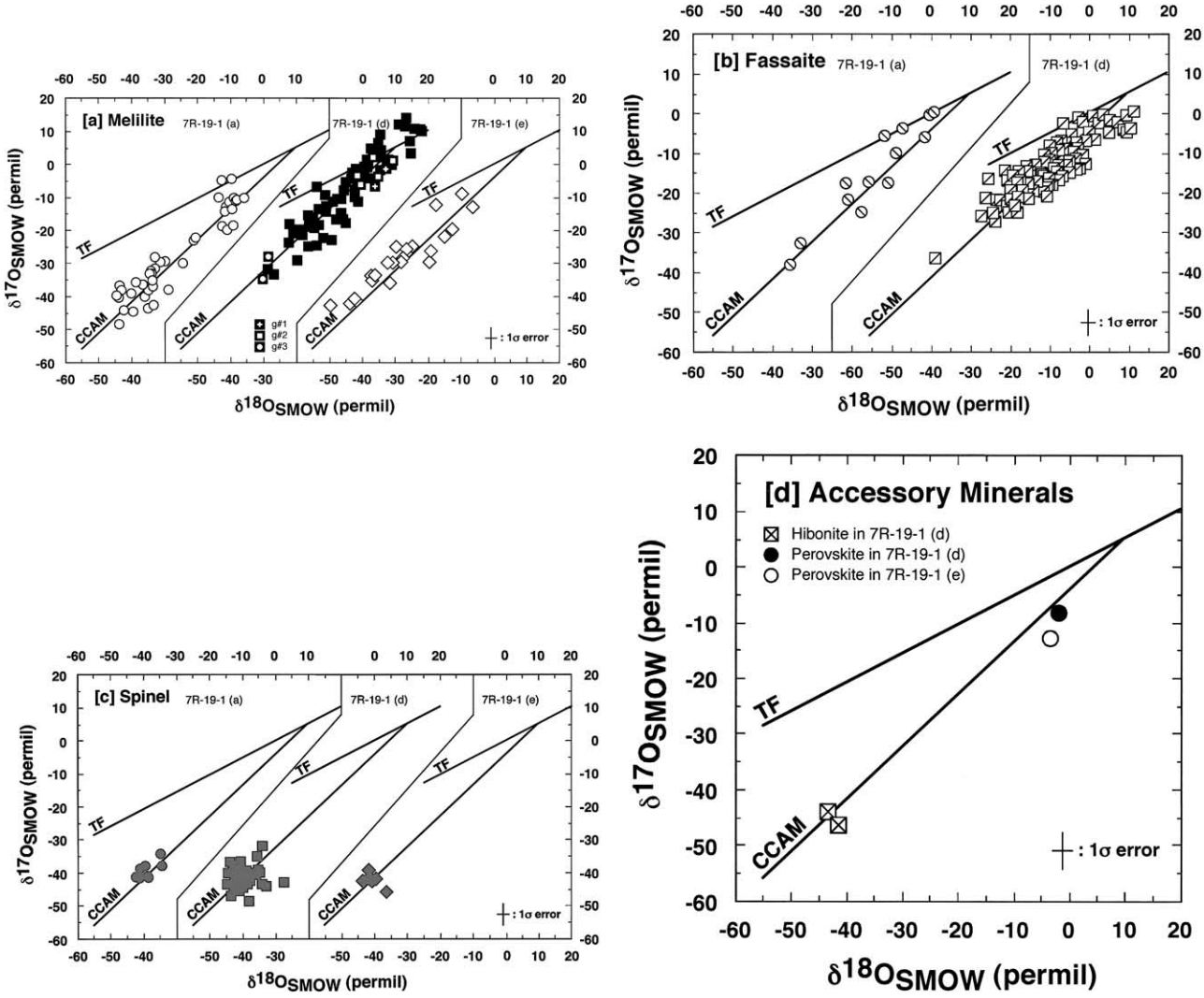

Fig. 8. Oxygen isotopic distributions of refractory minerals in 7R-19-1(a), (d), and (e). [a] For melilite, [b] for fassaite, [c] for spinel, and [d] for accessory minerals (hibonite and perovskite). TF = terrestrial fractionation line; CCAM = carbonaceous chondrites anhydrous minerals mixing line; SMOW = standard mean ocean water. Representative $1\sigma_{mean}$ error bars are shown.

rich melilite (Fig. 1 [a]). The textural relationship indicates that the spinel crystals were the first crystallized mineral in the CAI and that the spinel grains continued to crystallize during the crystallization of the ^{16}O-rich melilite. The observed texture is consistent with the O isotopic distribution in that both spinel grains and the surrounding melilite have the same O isotopic ratios. In 7R-19-1(d) and (e), on the other hand, spinel grains with ^{16}O-rich compositions are scattered throughout ^{16}O-poor melilite (Figs. 2 [a] and 3). After the crystallization of ^{16}O-poor melilite, O isotopic compositions of spinel enclosed in the melilite could not be changed from ^{16}O-poor to ^{16}O-rich. Therefore, ^{16}O-rich spinel grains were present before the crystallization of the surrounding ^{16}O-poor melilite.

4.2.2. O isotopic composition in melilite

The previous conclusion, combined with the observed uniform ^{16}O-enrichment in spinel, indicates that the formation of 7R-19-1 started under the condition of $\sim -21‰$ (Δ^{17}O) enrichment of ^{16}O relative to SMOW in the early solar system. In the three-oxygen isotope plots for 7R-19-1 (Fig. 8 [a]), there is a continuous distribution of O isotopic compositions of melilite ranging from $-40‰$ to $+10‰$ in $\delta^{17,\ 18}$O along the CCAM line. This suggests that the CAI was a) either initially produced with an ^{16}O-rich composition and exchanged O isotopes with the ^{16}O-poor environment in a later event, or b) was produced in an environment in which O isotope ratios were continuously changing.

Figure 9 [a] shows the traverse analysis at a grain boundary between ^{16}O-poor melilite (Mel) and ^{16}O-rich melilite (Mel*) crystals in 7R-19-1(a). The gehlenite-åkermanite ratios are similar in the core of both melilite crystals, but the O isotopic compositions differ. The åkermanite component in both is uniform within the central portion of each crystal, but it increases gradually toward the crystal rim (Fig. 9). From this

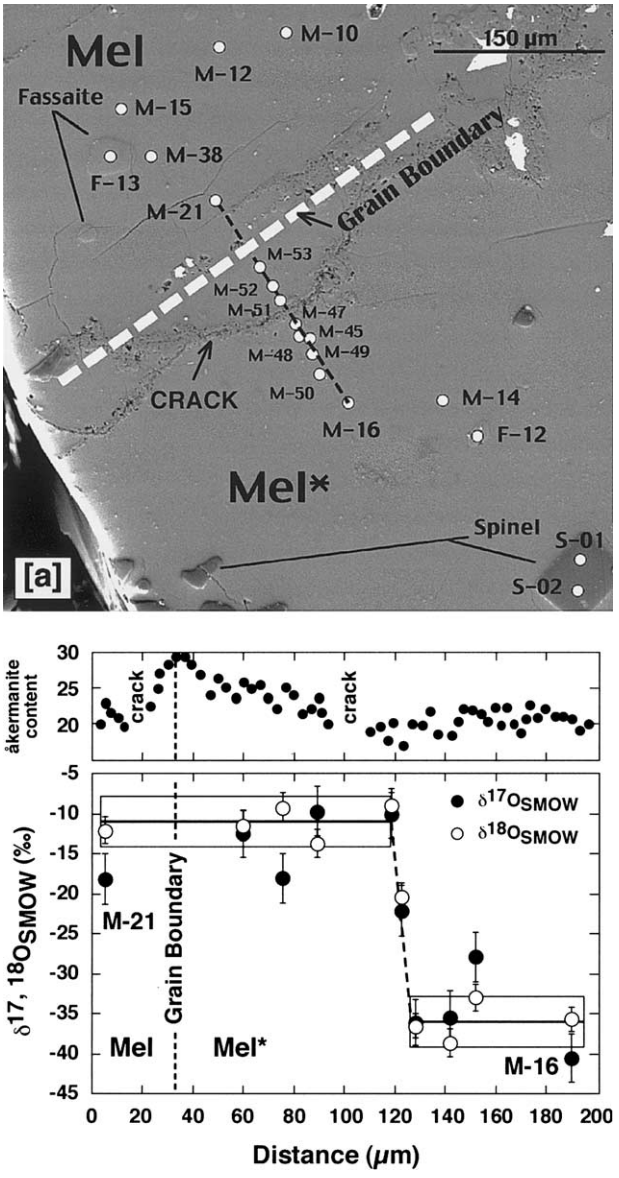

Fig. 9. Traverse analysis at the grain boundary between Mel (^{16}O-poor) and Mel* (^{16}O-rich) in 7R-19-1(a). [a] The line profile of O isotopic distribution shown in was obtained from stepped traverses across the boundary of the two melilite crystals. The line profile consisted of 10 points at intervals of ~15 μm. Open circles are analysis points. The grain boundary between Mel and Mel* is shown by the thick white dashed line. Numbers in the figure correspond to the measurement numbers in Tables 6, 7, and 8. Area shown is the boxed area [2] in Figure 1 [a]. Plot of the distribution of åkermanite content (mol%) and O isotopic ratios along the line between analytical locations M-16 and M-21. Solid and open circles are $\delta^{17}O_{SMOW}$ and $\delta^{18}O_{SMOW}$ values, respectively. Horizontal lines and boxes are averages and 1σ reproducibility, respectively, of $\delta^{18}O_{SMOW}$ within the area of homogeneous O isotopic ratios. The region enriched in ^{16}O is in sharp contact with the ^{16}O-poor region, but an obvious change in åkermanite content is not observed at the contact. The åkermanite content increases near and at the grain boundary. Error bars are 1σ_{mean}.

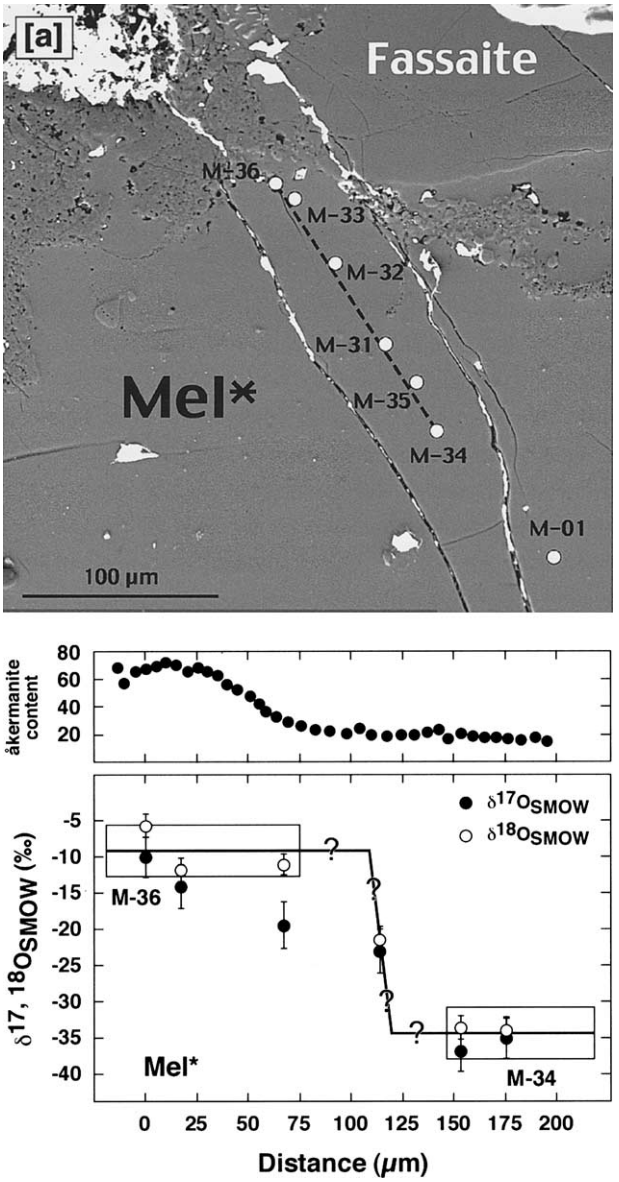

Fig. 10. Traverse analysis within Mel* (^{16}O-rich melilite) in 7R-19-1(a). [a] The line profile of O isotope distribution shown in was obtained from stepped traverses within the Mel* crystal. The line profile consisted of six points at intervals of ~25 μm. Open circles are analysis points. Numbers in the figure correspond to the measurement numbers of Table 6. Area shown is boxed area [3] in Figure 1 [a]. Plot of the distribution of åkermanite content (mol%) and O isotopic ratios along the line between analytical locations M-34 and M-36. Solid and open circles are $\delta^{17}O_{SMOW}$ and $\delta^{18}O_{SMOW}$ values, respectively. Horizontal lines and boxes are averages and 1σ reproducibility of $\delta^{18}O_{SMOW}$ within the areas of homogeneous O isotopic ratios, respectively. Error bars are 1σ_{mean}.

increase, it can be seen that melilite crystals grew towards the grain boundary from both sides. Although the O isotopic composition in Mel* is ^{16}O-enriched near the center of the crystal, it is deficient near the grain boundary. At the crystal rim, the composition is ^{16}O-poor to the same degree as in the adjacent Mel grain. ^{16}O-rich and ^{16}O-poor regions of Mel* are in direct contact within a single crystal, with a clear isotopic discontinuity. As the O isotopic compositions in the melilite plot on the CCAM line in Figure 8, the change of O isotopic compositions must be the result of the mixing of an ^{16}O-poor component with an ^{16}O-rich component.

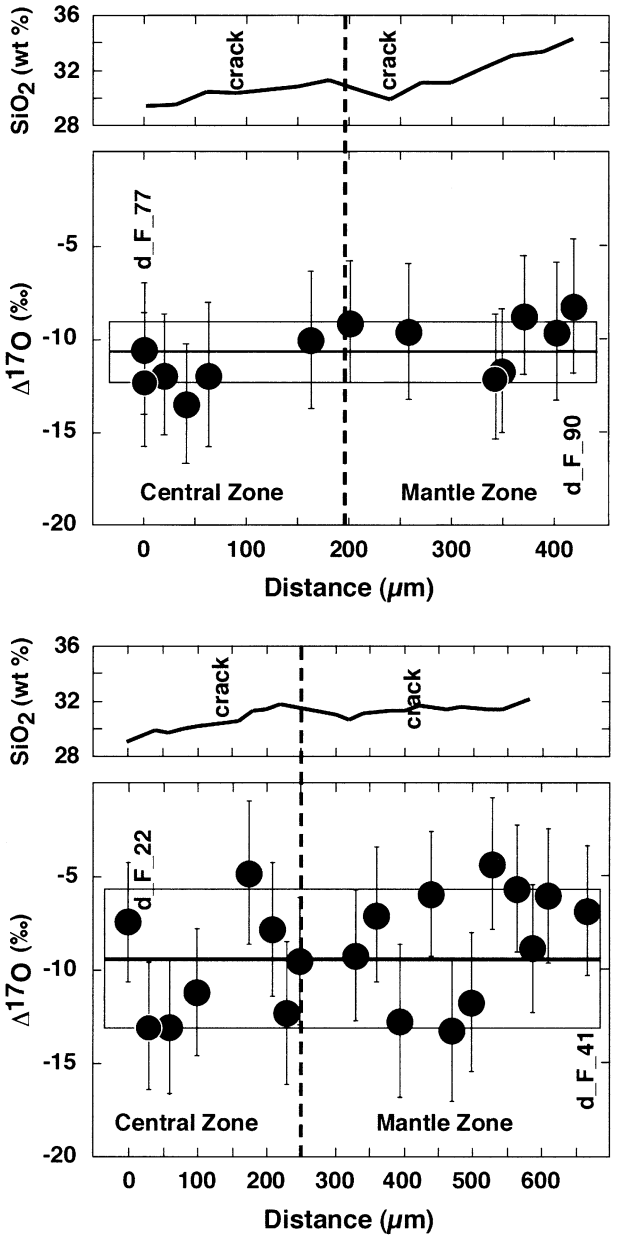

Fig. 11. Plot of the distribution of SiO_2 (wt%) in fassaite and $\Delta^{17}O$ along the lines between analytical locations at F-77 to F-90 as line profile 1 and F-22 to F-41 as line profile 2 in Figure 2 [b] and Table 6. Solid circles are $\Delta^{17}O$. Solid lines represent an average of $\Delta^{17}O$ values. Error bars are $1\sigma_{mean}$ and box is 1σ. Errors for $\Delta^{17}O$ were calculated from the error propagation from 1σ for $\delta^{18}O$ and $\delta^{17}O$.

Figure 10 [a] shows the traverse analysis within the ^{16}O-rich melilite, Mel*, near the angular fassaite crystal in the 7R-19-1(a). The åkermanite content gradually increases from the core to the rim (Fig. 10), whereas the core shows a uniform composition as in Mel* (Fig. 9). This zoning pattern indicates the crystal growth of melilite. O isotopic ratios change from −35‰ to −10‰ in $\delta^{17,\ 18}O$ in the uniform Åk content region where the Åk zoning starts. The position of O isotope change relative to the grain boundary is the same as in Mel* (Fig. 9).

A crack existed in the Mel* crystal in Figure 9 [a]. The position of the crack and that of the grain boundary are different. A possible explanation for the sharp O isotopic boundary between Mel* and Mel, namely that it is due to O isotopic exchange with an ^{16}O-depleted component penetrating through the crack, is ruled out because the O isotopic boundary does not correspond to the crack in Mel* (Fig. 9 [a]) nor is it along the crack in Figure 10 [a]. Therefore, it is difficult to envision O isotope exchange via cracks as the major cause for the O isotope heterogeneity in Mel*.

The observations of both line profiles also indicate that solid-state diffusion as a principal mechanism to generate the O isotopic heterogeneity between the Mel (^{16}O-poor melilite) and Mel* (^{16}O-rich melilite) grains is ruled out. If the change of O isotopic composition after crystallization is due to diffusion in the solid, O isotopic compositions should change gradually inside the crystal. Therefore, the ^{16}O-rich melilite must have crystallized before the crystallization of the ^{16}O-poor melilite, and the later-formed ^{16}O-poor melilite possibly results from remelting and recrystallizing caused by a reheating event. The O isotopic distributions in the melilite crystal can only be explained as the result of a sudden change from ^{16}O-rich to ^{16}O-poor during or before the recrystallization of O isotopic ratios in the surrounding environment.

Melilite with both ^{16}O-rich and ^{16}O-poor isotopic compositions formed in the solar nebula, as nebula gas with ^{16}O depletion and dust with ^{16}O enrichment existed simultaneously (Clayton, 1993). Our data indicate that ^{16}O-rich melilite crystallized without the O isotopic exchange with the surrounding solar nebula, and that ^{16}O-poor melilite crystallized after the exchange occurred. Possible candidates for the mechanism may be metamorphic recrystallization or solidification after remelting of precursor materials with ^{16}O-rich composition in an ^{16}O-poor environment during a subsequent reheating event. Because recrystallization of coarse-grained melilite is implausible during low-grade metamorphism on the Allende parent body, the ^{16}O-poor melilite probably resulted from remelting of the CAI in the solar nebula.

If this reheating event continued for a sufficiently long duration, O isotopic exchange by diffusion processes must have occurred across the ^{16}O-rich/^{16}O-poor boundary between different crystals (Fig. 9) and within the single crystal of melilite (Fig. 10). An upper limit of diffusion length indicated by Figure 10 is 80 μm, but the actual diffusion length is not well constrained by this value because of the wide distance between measurement points. In Figure 9, the O isotopic distribution is carefully measured in intervals every 5 μm around the boundary between regions of different O isotopic composition. The abrupt change of the O isotopic composition in Figure 9 strongly suggests that the possible diffusion length is 5 μm or less. As we classified 7R-19-1 as Type A, we may apply the experimental results of Stolper (1982). Since the crystallization temperature of melilite is at ~1400°C or higher for Type-A CAI (Stolper, 1982), the time for diffusing O distances of 5 μm and 80 μm are calculated to be less than 1 d and up to 17 d, respectively, using the diffusion coefficient for O in melilite (Yurimoto et al., 1989). Therefore, the short reheating duration for the formation of the CAI was less than 1 d. This diffusion length of melilite is too short to cause disturbance of O isotopic compositions of spinel and diopside and of the åkermanite composition of melilite because of their slow diffusivities (Ry-

erson and McKeegan, 1994; Nagasawa et al., 2001). These results for intramineral distributions of O isotopes support the view that the heterogeneous distribution of the O isotopic anomaly within the CAI was caused by multiple short-term heating events in the early solar nebula.

4.2.3. O isotopic compositions in fassaite

The O isotopic compositions observed in the angular fassaite crystal in 7R-19-1(a) (Fig. 1 [c]) vary from −15‰ to +1‰ in $\Delta^{17}O$ (Table 7). Such ^{16}O-poor fassaite is uncommon in normal CAIs (Clayton, 1993). If this O isotopic difference were caused by solid-state diffusion exchange with O of normal isotopic composition in the surrounding nebular gas, then the adjacent melilite crystal with higher diffusivity (Yurimoto et al., 1989; Ryerson and McKeegan, 1994) would not have been able to retain an ^{16}O-rich composition. Therefore, the observed variation of O isotopes cannot be explained by solid-state diffusion of O after crystallization of fassaite.

Several fine, rounded grains of fassaite (<20 μm in diameter) are scattered throughout the ^{16}O-rich melilite crystal in 7R-19-1(a) (Fig. 1 [a]). A single very small fassaite grain also was found in one spinel grain in 7R-19-1(d). These fassaite grains ($\Delta^{17}O = \sim -17$‰, Table 7) appear to have been trapped in the melilite or spinel and, judging by their rounded shape, may be a relict phase from the CAI precursor. They are enriched in ^{16}O to the same degree as the surrounding ^{16}O-rich melilite ($\Delta^{17}O$ for Mel* = ∼ −18‰, Table 6).

Elsewhere within sample 7R-19-1(a), small (<30 μm in diameter) fassaite grains exist in ^{16}O-poor melilite crystals. A fassaite grain in this setting was found to be slightly richer in the ^{16}O-rich component ($\Delta^{17}O = \sim -8$‰, Table 7) than the surrounding ^{16}O-poor melilite ($\Delta^{17}O$ for Mel = ∼ −5‰, Table 6). The similarity in the O isotopic composition of the fine-grained fassaite in the ^{16}O-poor melilite and the angular fassaite in 7R-19-1(a) suggests that the angular fassaite and the fine-grained fassaite in the ^{16}O-poor melilite crystallized before the ^{16}O-poor melilite crystallized.

The line profiles for $\Delta^{17}O$ in the large, angular fassaite of 7R-19-1(d) are relatively homogeneous (Fig. 11) from core to rim. These near-constant O isotopic ratios indicate that the O isotopic composition in the CAI melt did not change during the crystallization of this fassaite. Observations of the oxide abundance within this crystal (Fig. 7), however, show that the angular fassaite has separate core and mantle parts. We therefore suggest that this fassaite crystallized from a melt with evolving chemical compositions before the O isotopic compositions of the melt changed. Even if there is growth zoning, as represented by the sharp boundary of chemical compositions in the crystal, a change in the O isotopic compositions in the crystal is not indicated.

Based on the O isotopic measurement of fassaite crystals in 7R-19-1, fassaites having various O isotopic compositions were preserved in the CAI. These O isotopic variations indicate that the fassaites consist of crystals formed from various origins, such as surviving relict phases of the CAI precursor, and that they crystallized after the melting of the CAI precursor.

4.2.4. O isotopic compositions of perovskite

We have measured O isotopic compositions of fine-grained perovskite crystals in the central part of 7R-19-1(d) and in the rim of 7R-19-1(e) (Table 9). The measured perovskite crystal in the center area of 7R-19-1(d) was mainly surrounded by aggregates of spinel and hibonite crystals with identical ^{16}O-enrichments (Tables 8 and 9). However, the perovskite has an ^{16}O-poor isotopic composition. The perovskite crystal in the rim of 7R-19-1(e) is surrounded by spinel crystals and also is ^{16}O-poor compared to these (Tables 8 and 9). In other words, the perovskite crystals in the rim and central area have the same O isotopic compositions of $\Delta^{17}O = \sim -10$‰, which is different from what is observed in surrounding minerals. O diffusivity in perovskite is ∼3 to 6 orders of magnitude higher than that in other minerals from CAIs: spinel, anorthite, diopside, åkermanite and gehlenite (Yurimoto et al., 1989; Gautason and Muehlenbachs, 1993; Ryerson and McKeegan, 1994). Since perovskite grains are the smallest crystals among the CAI minerals, their O isotope ratios are comparatively easy to change from their original ratios to ^{16}O-depleted values during parent-body processes.

4.3. Formation Process of 7R-19-1

Based on the O isotopic distributions among CAI constituent minerals, chemical compositions of minerals and petrographic textures, the crystallization sequence of 7R-19-1 can be traced. Initially, spinel and melilite crystallized from a Ca, Al-rich silicate liquid enriched in ^{16}O by ∼ 40‰ relative to the terrestrial isotope ratio. Following spinel and melilite, fassaite started to crystallize from the residual liquid. The crystallization sequence determined by Stolper (1982) is parallel to the order of the O isotopic anomalies among these minerals. O isotopic compositions in melilite vary widely from −40‰ to 0‰ in $\delta^{17,\ 18}O$ (Fig. 8 [a]). This means that ^{16}O-rich melilite experienced multiple remelting/recrystallizing episodes and O isotopic ratios in melilite gradually evolved to become less ^{16}O-rich. The melilite crystals with more evolved O isotopic compositions crystallized simultaneously with the fassaite. Because the chemical compositions of the core of ^{16}O-poor melilite and of the adjacent ^{16}O-rich melilite are similar and the O isotopic distribution changes sharply from ^{16}O-rich to ^{16}O-poor, it is difficult to explain how the ^{16}O-poor melilite was sequentially crystallized by a single stage of cooling. Before, or during, the crystallization of ^{16}O-poor melilite, fassaite crystals with various O isotopic compositions formed. During the crystallization of the fassaite grains, an event which changed the chemical composition of the CAI liquid occurred: possibly a mixing of a melilite component into the CAI liquid. Results of the line analyses of O isotopes within the fassaite crystals indicate that the fassaite crystallized from a liquid with homogeneous O isotopic ratios.

One potential problem with this remelting model is that fassaite grains should melt first according to the phase equilibrium diagram for CAI compositions. Thus, relict fassaite grains with ^{16}O enrichment are unlikely to remain. However, for transient heating, melting of minerals may be controlled by kinetics rather than by equilibrium. According to a model for the kinetics of congruent melting, the melting rate of åkerman-

ite is much faster than that of diopside at temperatures above the melting point of åkermanite (Greenwood and Hess, 1996). At 1600°C, when åkermanite and diopside have the same grain size, melting of åkermanite is faster than that of diopside by about one and half orders of magnitude (Greenwood and Hess, 1996). As the grain size of melilite is similar to that of the angular fassaite in 7R-19-1, melilite grains would have melted faster than the fassaite grains. Based on the results of O isotope measurements in melilite and fassaite, after the transient heating, melilite and fassaite grains again crystallized from the liquid produced by remelting of preexisting minerals. The REE distributions among fassaite,^{16}O-rich melilite and ^{16}O-poor melilite crystals in 7R-19-1(a) are also consistent with a process of partial remelting (Yurimoto et al., 1998).

Rather than being unique, the formation process of 7R-19-1 can be applied to other CAIs. If CAI precursors were composed originally of ^{16}O-rich materials, remelting would result in O isotopic similarity between the surrounding nebular gas and the newly crystallized minerals. If the reheating event occurred one or more times during CAI formation (e.g., Yurimoto et al., 1989; Sheng et al., 1992; MacPherson and Davis, 1993; Ryerson and McKeegan, 1994), the O isotopic composition of CAIs would be reset to the solar nebular value except in the unmelted portions of crystals. At least one remelting/recrystallizing process is necessary to explain the existence of the sharp O isotopic boundary within the ^{16}O-rich melilite crystals. Moreover, it is necessary that the large variations in O isotopic compositions of melilite and fassaite were formed by successive, multiple remelting/recrystallizing events. The heterogeneous O isotopic distribution among minerals having igneous textures like normal Allende Type B CAI could result from such multiple heating events. A possible candidate for the energy source of the multiple heating events may be fluctuating radiation of an active protosun (Shu et al., 1997; Itoh and Yurimoto, 2003).

5. CONCLUSIONS

Oxygen isotope ratios ^{18}O/^{16}O and ^{17}O/^{16}O were measured by SIMS with 5 μm lateral resolution in minerals from Allende CAI 7R-19-1. these ratios fall along the slope of the $\sim$ 1 CCAM line. The major refractory minerals (spinel, fassaite and melilite) showed large negative anomalies of ^{17}O and ^{18}O relative to ^{16}O, and the order of O isotopic anomalies is parallel to the crystallization sequence from a CAI compositional liquid. This indicates that the CAIs crystallized from a liquid of CAI composition. Although the degree of the O isotope anomalies in 7R-19-1 and the normal coarse-grained CAIs are different, lower limit values of Δ^{17}O are similar at about -21‰ relative to the terrestrial value. The similarity in the extreme values demonstrates that the crystallization of all CAIs started from a Ca, Al-rich liquid with an ^{16}O-rich composition of ~ -21‰ (Δ^{17}O). Sharp O isotopic boundaries within and between melilite crystals indicate that 7R-19-1 experienced incomplete remelting caused by at least one reheating event of approximately 1 d. This remelting process occurred in an ^{16}O-poor isotopic environment because the recrystallized material is ^{16}O-depleted. Fassaite crystals consist of aggregates of various origins, such as relict CAI precursors. They crystallized from a CAI melt which had various O isotopic compositions established during remelting. The heterogeneous O isotopic distributions among minerals having the igneous texture of normal CAIs could result from the multiple heating events.

The ^{16}O-poor isotopic compositions cannot result from solid-state diffusion, i.e., O isotopic exchange between the unmelted minerals and surrounding gas did not occur even at the time of partial remelting of CAI precursors. The coexistence of igneous minerals with O isotopic distributions in disequilibrium may be explained as a result of gradual isotope exchange between partially molten CAI droplets with ^{16}O-rich isotopic compositions and the surrounding solar nebula gas with ^{16}O-poor composition during successive multiple heating events.

Acknowledgments—The 7R-19-1 samples were provided by Dr. Elbert King. MI would like to thank Dr. Robert Ilchik and Prof. Roy Johnson for critical discussion and for help in improving the English of this paper. Comments and suggestions by an anonymous reviewer, Dr. J. Paque, Dr. F. J. Ryerson and associate editor Dr. U. Ott resulted in significant improvement to the paper and are gratefully acknowledged. This work was partly supported by Monbu-Kagaku-Gijutsu Sho (HY and HN).

Associate editor: U. Ott

REFERENCES

Allègre C. J., Manhès G., and Göpel C. (1995) The age of Earth. *Geochim. Cosmochim. Acta* **59,** 1445–1456.

Ando K. and Oishi Y. (1974) Self-diffusion coefficients of oxygen ion in single crystals of MgO · nAl_2O_3 spinels. *J. Chem. Phys.* **61,** 625–629.

Beckett J. R. (1986) The origin of calcium-, aluminum-rich inclusions from carbonaceous chondrite: An experimental study. Ph.D. thesis. University of Chicago.

Clayton R. N. (1993) Oxygen isotopes in meteorites. *Annu. Rev. Earth Planet. Sci.* **21,** 115–149.

Clayton R. N., Grossman L., and Mayeda T. K. (1973) A component of primitive nuclear composition in carbonaceous meteorite. *Science* **182,** 485–488.

Clayton R. N. and Mayeda T. K. (1977) Correlated oxygen and magnesium isotope anomalies in Allende inclusions. I: Oxygen. *Geophy. Res. Lett.* **4,** 295–298.

Clayton R. N., Onuma N., Grossman L., and Mayeda T. K. (1977) Distribution of the pre-solar component in Allende and other carbonaceous chondrites. *Earth Planet. Sci. Lett.* **34,** 209–224.

Davis A. M., MacPherson G. J., Clayton R. N., Mayeda T. K., Sylvester P. J., Grossman L., Hinton R. W., and Laughlin J. R. (1991) Melt solidification and late-stage evaporation in the evolution of a FUN inclusion from the Vigarano C3V chondrite. *Geochim. Cosmochim. Acta* **55,** 621–637.

De Chambost E., Schuhmacher M., Lovestam G., and Claesson S. (1991) Achieving high transmission with the Cameca IMS 1270. In *Secondary Ion Mass Spectrometry SIMS X* (eds. B. B. Hagenhoff and H. W. Werner), pp. 1003–1006. Wiley.

Fahey A. J., Goswani J. N., McKeegan K. D., and Zinner E. K. (1987) ^{16}O excesses in Murchison and Murray hibonites: A case against a late supernova injection origin of isotopic anomalies in O, Mg, Ca and Ti. *Astrophys. J. (Lett.)* **323,** L91–L95.

Gautason B. and Muehlenbachs K. (1993) Oxygen diffusion in perovskite: Implications for electrical conductivity in the lower mantle. *Science* **260,** 518–521.

Greenwood J. P. and Hess P. C. (1996) Congruent melting kinetics: Constraints on chondrule formation. In *Chondrules and the Plotoplanetary Disk* (eds. R. H. Hewkins, R. H. Jones, and E. R. D. Scott), pp. 205–211. Cambridge University Press.

Grossman L. (1972) Condensation in the primitive solar nebula. *Geochim. Cosmochim. Acta* **36,** 597–619.

Grossman L. (1975) Petrography and mineral chemistry of Ca-rich inclusions in the Allende meteorite. *Geochim. Cosmochim. Acta* **39,** 433–454.

Hayashi T. and Muehlenbachs K. (1986) Rapid oxygen diffusion in melilite and its relevance to meteorites. *Geochim. Cosmochim. Acta* **50,** 585–591.

Ito M. (1999) Oxygen isotopic microanalysis by SIMS: A study of the formation process and thermal history of the Allende meteorite in the early solar system. Ph.D. thesis. Gakushun University.

Itoh S. and Yurimoto H. (2003) Contemporaneous formation of chondrules and refractory inclusions in the early solar system. *Nature* **423,** 728–731.

Kobayashi S., Imai H., and Yurimoto H. (2003) New extreme ^{16}O-rich reservoir in the early solar system. *Geochem. J.* **37,** 663–669.

MacPherson G. J., Wark D. A., and Armstrong J. T. (1988) Primitive material surviving in chondrites: Refractory inclusions. In *Meteorites and the Early Solar System* (eds. J. F. Kerridge and M. S. Matthews), pp. 746–807. University of Arizona Press.

MacPherson G. J. and Davis A. M. (1993) A petrologic and ion microprobe study of a Vigarano Type B refractory inclusion: Evolusion by multiple stages of alteration and melting. *Geochim. Cosmochim. Acta* **57,** 231–243.

MacPherson G. J., Davis A. M., and Zinner E. K. (1995) The distribution of aluminum-26 in the early solar system—A reappraisal. *Meteoritics* **30,** 365–377.

McKeegan K. D. (1987) Oxygen isotopes in refractory stratospheric dust particles: Proof of extraterrestrial origin. *Science* **237,** 1468–1471.

McKeegan K. D., Leshin L. A., Russell S. S., and MacPherson G. J. (1998) Oxygen isotopic abundances in calcium-aluminum-rich inclusions from ordinary chondrites: Implications for nebular heterogeneity. *Science* **280,** 414–418.

Nagasawa H., Suzuki T., Ito M., and Morioka M. (2001) Diffusion in single crystal of melilite: Interdiffusion of Al + Al vs. Mg + Si. *Phys. Chem. Minerals* **28,** 706–710.

Ryerson F. J. and McKeegan K. D. (1994) Determination of oxygen self-diffusion in åkermanite, anorthite, diopside, and spinel: Implications for oxygen isotopic anomalies and the thermal histories of Ca-Al–rich inclusions. *Geochim. Cosmochim. Acta* **58,** 3713–3734.

Sheng Y. J., Wasserburg G. J., and Hutcheon I. D. (1992) Self diffusion of magnesium in spinel and in equilibrium melts: Constraints on flash heating of silicates. *Geochim. Cosmochim. Acta* **56,** 2535–2546.

Shu F. H., Shang H., Glassgold A. E., and Lee T. (1997) X-rays and fluctuating X-wind from protostars. *Science* **277,** 1475–1479.

Simon S. B., Grossman L., and Davis A. M. (1991) Fassaite composition trends during crystallization of Allende Type B refractory inclusion melts. *Geochim. Cosmochim. Acta* **55,** 2635–2655.

Simon S. B., Davis A. M., and Grossman L. (1995) Crystallization of compact Type A refractory inclusions: Implications from crystal zoning and trace element distribution. *Lunar Planet. Sci.* **26,** 1303–1304.

Simon S. B., Davis A. M., and Grossman L. (1999) Origin of compact Type A refractory inclusions from CV3 carbonacaous chondrites. *Geochim. Cosmochim. Acta* **63,** 1233–1248.

Stolper E. (1982) Crystallization sequences of Ca-Al–rich inclusions from Allende: An experimental study. *Geochim. Cosmochim. Acta* **46,** 2159–2180.

Stolper E. and Paque J. M. (1986) Crystallization sequences of Ca-Al–rich inclusions from Allende: The effect of cooling rate and maximum temperature. *Geochim. Cosmochim. Acta* **50,** 1785–1806.

Wark D. A. (1981) The pre-alteration compositions of Allende Ca-Al–rich condensates. *Lunar Planet. Sci.* **12,** 1148–1150.

Wark D. A. (1987) Plagioclase-rich inclusions in carbonaceous chondrite meteorites: Liquid condensates? *Geochim. Cosmochim. Acta* **51,** 221–242.

Wark D. A., Boynton W. V., Keays R. R., and Palme H. (1987) Trace element and petrologic clues to the formation of forsterite-bearing Ca-Al–rich inclusions in the Allende meteorite. *Geochim. Cosmochim. Acta* **51,** 607–622.

Yurimoto H., Morioka M., and Nagasawa H. (1989) Diffusion in single crystals of melilite: I. *Oxygen. Geochim. Cosmochim. Acta* **53,** 2387–2394.

Yurimoto H., Nagasawa H., Mori Y., and Matsubaya O. (1994) Microdistribution of oxygen isotopes in a refractory inclusion from the Allende meteorite. *Earth Planet. Sci. Lett.* **128,** 47–53.

Yurimoto H., Ito M., and Nagasawa H. (1998) Oxygen isotope exchange between refractory inclusion in Allende and solar nebula gas. *Science* **282,** 1874–1877.

Zinner E. K., Caillet C., and EL Goresy A. (1991) Evidence for extraneous origin of a magnesiowüstite-metal Fremdling from the Vigarano CV3 chondrite. *Earth Planet. Sci. Lett.* **102,** 252–264.